



Estimation of daily evapotranspiration and irrigation water efficiency at a Landsat-like scale for an arid irrigation area using multi-source remote sensing data



Yanfei Ma^{a,b}, Shaomin Liu^{a,*}, Lisheng Song^c, Ziwei Xu^a, Yaling Liu^d, Tongren Xu^a, Zhongli Zhu^a

^a State Key Laboratory of Earth Surface Processes and Resource Ecology, Faculty of Geographical Science, Beijing Normal University, Beijing 100875, China

^b Department of Geography, Handan College, Hebei 056005, China

^c School of Geographical Sciences, Southwest University, Chongqing 400712, China

^d Department of Earth and Environmental Engineering, Columbia University, New York, NY 10027, USA

ARTICLE INFO

Keywords:

Evapotranspiration
Multi-source remote sensing
Fusion
Landsat-like scale
SEBS
Eddy covariance system
Irrigation water efficiency
Heihe River Basin

ABSTRACT

The estimation of land-surface evapotranspiration (ET) at high spatial and temporal resolutions is important for management and planning of agricultural water resources, but available remote sensing data generally have either high spatial resolution or high temporal resolution. To overcome this limitation, we evaluated the use of a data fusion scheme, Enhanced Spatial and Temporal Adaptive Reflectance Fusion Model (ESTARFM), to determine the surface parameters needed to estimate daily ET at a Landsat-like scale (100 m). In particular, we fused Moderate Resolution Imaging Spectroradiometer (MODIS) data with Landsat Enhanced Thematic Mapper Plus (ETM+) data in analysis of the Heihe River Basin (HRB), an arid region of Northwest China. The surface parameters were then used to drive the revised Surface Energy Balance System (SEBS) model to estimate daily ET at a spatial resolution of 100 m for this an arid irrigation area during the crop growth period (April to October) in 2012. The results showed that the daily ET estimates had a mean absolute percent error (MAPE) of 12% and a root mean square error (RMSE) of 0.81 mm/day relative to ground measurements from 18 eddy covariance (EC) sites in the study area. The validation results indicated good accuracy for land cover types of maize and vegetables, a slight overestimation for residential and wetland sites, and a slight underestimation for orchard site. Our comparison of the input parameter fusion approach (IPFA) and the ET fusion approach (ETFA) with field measurements indicated the IPFA was superior than the ETFA for land surfaces with high spatial heterogeneity. Furthermore, our high spatiotemporal ET estimates indicated that irrigation water efficiencies of the irrigation districts (mean: 70%) and villages (mean: 62%) had large spatial heterogeneity. These results point to the need for calculating ET at a high spatiotemporal resolution for monitoring and improving irrigation water efficiency at local scales. Our findings suggest that the proposed framework of estimating daily ET at a Landsat-like scale using multi-source data may also be applicable to other heterogeneous landscapes by providing a foundation for management of water resources at the basin or finer scales.

1. Introduction

Irrigation accounts for approximately 70% of the world's total freshwater withdrawals (WWAP, 2016). Agricultural production in arid and semi-arid areas usually requires irrigation, and these regions consume approximately 80% to 95% of the total freshwater used for irrigated agriculture in Western Europe (Battude et al., 2017), Western Asia (Elnesr and Alazba, 2013), and Northwest China (Chen et al., 2003). Irrigation water efficiency is a measure of the effectiveness of irrigation that researchers commonly use to characterize farm lands

(Ahadi et al., 2013). As fresh water has become increasingly scarce in many regions of the world, it is important to improve the efficiency of irrigation. Additionally, quantifying current irrigation water efficiency can provide a basis for improving efficiency and the management of water resources.

Quantification of irrigation water efficiency at the field scale first requires accurate and high spatiotemporal resolution estimates of surface evapotranspiration (ET) (Bastiaanssen et al., 2005; Anderson et al., 2007; Allen et al., 2008; Yang et al., 2012; Anderson et al., 2012a,b; Cammalleri et al., 2008, 2013; Wu et al., 2015; Zayed et al., 2016;

* Corresponding author.

E-mail address: smliu@bnu.edu.cn (S. Liu).

Senay et al., 2016; Bai et al., 2017), and these measurements can provide a basis for making decisions regarding irrigation management (Fereres and Soriano, 2007; Fraiture and Wichelns, 2010; Martin et al., 2013). Satellite sensors, such as the Moderate Resolution Imaging Spectroradiometer (MODIS), the Advanced Very High Resolution Radiometer (AVHRR), and the Visible Infrared Imaging Radiometer (VIIRS) provide daily thermal infrared (TIR) data, but their resolutions (~ 1 km) are too coarse for estimation of ET at the field scale (Bastiaanssen et al., 2001; Allen et al., 2008; Cammalleri et al., 2013, 2014a,b; Wu et al., 2015). On the other hand, the Landsat 5 Thematic Mapper (TM)/7 Enhanced Thematic Mapper Plus (ETM+)/8 Thermal Infrared Sensor (TIRS) and the Terra Advanced Spaceborne Thermal Emission and Reflection Radiometer (ASTER) provide high spatial resolution thermal infrared (TIR) data (approximately 100 m), but they have a lengthy return interval, and cloud cover can interfere with image acquisition. Therefore, a method that combines the fine spatial resolution of Landsat-like data and the high temporal resolution of MODIS-like data will provide significant benefits for water resource management at the field scale (Cammalleri et al., 2013, 2014a,b). Previous studies have proposed several methods to overcome the limitations of these imaging methods for estimation of regional ET at high spatiotemporal resolutions: Thermal sharpening (Kustas et al., 2003; Bindhu et al., 2013; Agam et al., 2007, 2008), simple output disaggregation models (Hong et al., 2011; Eswar et al., 2013, 2017), and data fusion (Cammalleri et al., 2013, 2014a,b; Bai et al., 2017).

In general, two strategies can perform data fusion to estimate ET at high spatiotemporal resolution using data fusion method. One method is the ET fusion approach (ETFA), in which MODIS- and Landsat-derived ET maps are fused to compensate for their spatial and temporal resolutions, respectively. Previous studies have used the ETFA to estimate daily ET in fields of rain-fed and irrigated corn, soybean, and cotton (Cammalleri et al., 2013, 2014a,b), and irrigated vineyards (Semmens et al., 2016). Additionally, Bai et al. (2017) integrated MODIS ET (250 m, daily) and Landsat ET to produce daily field-scale ET data in the western part of the Hetao Irrigation District of North China. Another method is the input parameter fusion approach (IPFA). This method fuses spectral reflectance and radiance observations from multiple satellite sensors to derive the physical parameters of the land surface (albedo, emissivity, land surface temperature [LST], and vegetation coverage), and then uses these parameters as inputs for ET models.

Previous studies have successfully applied two data fusion algorithms for ETFA: The Spatial and Temporal Adaptive Reflectance Fusion Model (STARFM) (Gao et al., 2006; Cammalleri et al., 2013, 2014a,b) and the enhanced STARFM (ESTARFM) (Zhu et al., 2010; Bai et al., 2017). Both algorithms identify spatial variations from high spatial resolution images and examine temporal changes from high temporal resolution images to produce new simulated images (Gao et al., 2006, 2017; Zhu et al., 2010). Emelyanova et al. (2013) proposed a framework for selection of blending algorithms based on partitioning of the spatial and temporal variances and suggested that ESTARFM was a superior blending algorithm when the spatial variance in the relevant spectral bands was predominant. Jarihani et al. (2014) found that STARFM had better accuracy when the temporal variance was higher than the spatial variance ($\sigma_t^2/\sigma_s^2 > 1$), but ESTARFM had typically had better accuracy when the spatial variance was higher ($\sigma_t^2/\sigma_s^2 < 1$).

Over the last two decades, many studies have used the surface energy balance method to estimate ET for irrigated agricultural areas worldwide (Bastiaanssen et al., 2001; Allen et al., 2005; Droogers et al., 2010; Liou and Kar, 2014; Senay et al., 2016; Bai et al., 2017). The Surface Energy Balance System (SEBS) model (Su, 2002) is one of the most widely used one-source energy balance models. This model uses a sequence of physically-based equations (Su et al., 2001; Su, 2002) to estimate ET rates at local and regional scales (Jia et al., 2003; Su et al., 2005; Chen et al., 2014). However, the SEBS model may underestimate the sensible heat flux (McCabe and Wood, 2006; Choi et al., 2009;

Timmermans et al., 2013; Chirouze et al., 2014; Ma et al., 2015). Moreover, previous studies have reported uncertainties of the SEBS model, and the need for modifications when it is implemented at local and regional scales (Gokmen et al., 2012; Chen et al., 2013a,b). For example, to improve ET estimates over heterogeneous oasis-desert surfaces in the midstream of the Heihe River Basin (HRB) of Northwest China, Ma et al. (2015) used ground measurements to modify several key parameters of the SEBS model by using ground measurements. Clearly, given the possible sensitivity of the model outputs to the “model physics” and parameterization schemes, calibration of the model using ground observations improves its performance at the scale of the observations (Liu et al., 2007a,b; Liu et al., 2013, 2014, 2015; Yang et al., 2008; Chen et al., 2013a; Mallick et al., 2014, 2015, 2016; Wang et al., 2018).

The Heihe River Basin (HRB) is one of the most hydrologically vulnerable areas worldwide, and is typical of many arid and semi-arid regions (Cheng et al., 2014). Recently, water scarcity and conflicts among users have become more intense in the HRB due to the increasing use of irrigation water by the midstream regions and the environmental flow requirements of the downstream regions (Cheng et al., 2014). As a first step toward resolving these conflicts for the HRB, it is necessary to examine irrigation water efficiency at high spatiotemporal resolution in this region (Li et al., 2018). In addition, an analysis of the rich experimental data in the HRB (Li et al., 2013, 2018) will allow this area to serve as a testbed for additional examinations of water-related issues in other arid and semi-arid regions.

ET is a required input for calculation of irrigation water efficiency. Thus, estimations of ET at a high spatiotemporal resolution are needed to determine irrigation water efficiency at high spatiotemporal resolution. We produced daily Landsat-like scale ET data for the HRB area by deploying the SEBS model and fusing multiple sources of satellite remote sensing data with ground measurements in the HRB. This work is a necessary first step toward resolving water conflicts in the HRB area. Our specific objectives were to: (i) estimate and validate daily ET at a Landsat-like scale for the midstream irrigated area of the HRB using a multi-source remote sensing data fusion method (ESTARFM) with the revised SEBS model; (ii) analyze the spatiotemporal variations in the ET estimates; and (iii) assess the irrigation water efficiency for the different irrigation districts and villages using the ET estimates. The research framework employed here could be applicable to other arid and semi-arid regions, and our specific findings could also provide a basis for water resource management practices in these other regions.

2. Experiments and data

2.1. Study area and HiWATER-MUSOEXE experiments

The HRB covers an area of approximately 143,000 km² in the arid region of Northwest China (Fig. 1, left). It is the second largest inland river basin in China and has various types of land cover. The HRB is dry and has strong winds, high solar radiation, and large daily temperature variations. The annual average stream flow measured at the Yingluo gauge (outlet from upstream) was 15.97×10^8 m³ from 1945 to 2012. In the midstream of the HRB, the main crop is maize, and the limited water resources are mainly used by the irrigated oasis, which covers approximately 12% of the entire HRB. This area has become an important source of commodity grains in Northwest China. Irrigation water in the HRB is primarily from the surface water of the main stream of the Heihe River, and there are supplemental withdrawals from groundwater sources.

The study area (90 km × 90 km) is in the midstream of the HRB. This area covers 12 irrigation districts (Fig. 1, right; Shangsan, Daman and Yingke, Ganjun, Xigan, Shahe, Wujiang, Yanuan, Banqiao, Pingchuan, Liaoquan, and Liyuan River) and has > 4000 pumping wells. The soil is mainly loam in the irrigation districts, and is mixed loam and sand in the barren desert.

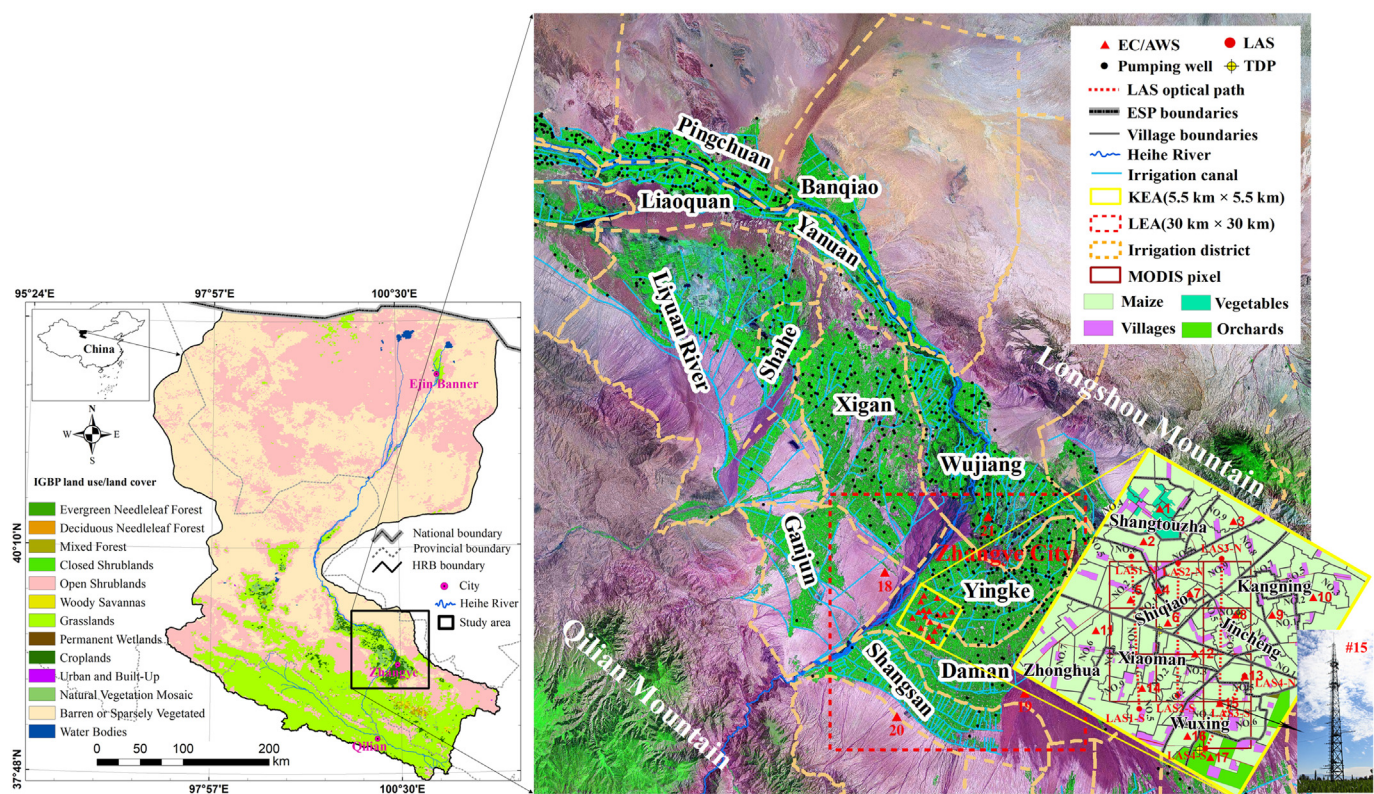


Fig. 1. Left: Land use and land cover of the Heihe River Basin (HRB) in Northwest China, and location of the 90 km × 90 km study area. Right: False color composite of Landsat image mosaicked from the Landsat GeoCover dataset (MDA Federal, 2004), showing the two nested matrices (Large Experimental Area [LEA]: red dashed box, 30 km × 30 km; Kernel Experimental Area [KEA]: yellow box, 5.5 km × 5.5 km) and the irrigated area in the midstream of HRB. Observation sites are also shown. Abbreviations: EC/AWS, eddy covariance system (EC)/automatic weather station (AWS); LAS, large-aperture scintillometer; TDP, thermal dissipation sap flow probes. (For interpretation of the references to color in this figure legend, the reader is referred to the web version of this article.)

The Heihe Watershed Allied Telemetry Experimental Research (HiWATER) program was designed as a comprehensive ecohydrological experiment within the framework of the Heihe Plan. This program considers the diverse needs of this region and uses the existing observational infra-structure of the HRB. The “Multi-Scale Observation Experiment on Evapotranspiration over heterogeneous land surfaces 2012” (HiWATER-MUSOEXE), which is part of the HiWATER, was the first thematic experiment in the HRB (Li et al., 2013). HiWATER-MUSOEXE used a flux observation matrix, consisting of two nested matrices in the midstream of the HRB, between May and September in 2012. A Large Experimental Area (LEA, 30 km × 30 km) was in an oasis-desert area, and a Kernel Experimental Area (KEA, 5.5 km × 5.5 km) was inside the oasis (Fig. 1, right). The LEA (Fig. 1, red dashed box) contains a cross-shaped observational arrangement that includes one superstation (Daman Superstation [#15]) and four ordinary stations (Bajitan Gobi station [#18], Shenshawo sandy desert station [#19], Huazhaiizi desert steppe station [#20], and Zhangye wetland station [#21]). The KEA was entirely within the LEA (Fig. 1, yellow box) and has 17 elementary sampling plots (ESP) (vegetables [#1], villages [#4], orchards [#17], and maize [#2, #3, #5 to #16]) that were established based on land use (crops, shelterbelts, residential areas, roads, and canals), soil moisture and irrigation status. Each ESP has one automatic weather station (AWS) and one eddy covariance (EC) system. A total of 21 AWSs (4 around the oasis) and 22 EC systems (2 at site #15) were installed in the experimental area. In addition, 4 large-aperture scintillometer (LAS) systems were installed in three 3 × 1 and one 2 × 1 MODIS pixels to measure sensible heat flux at the satellite pixel scale. Thermal dissipation sap flow probes (TDPs) were installed in trees of different heights and diameters at 3 sites in the shelter belt for measurements of transpiration. Xu et al. (2013), Liu et al. (2016), and Li et al. (2017) provided details of the HiWATER-MUSOEXE field

measurements and the HiWATER-MUSOEXE multiscale dataset. The flux observation matrix data were used to validate estimations of daily ET at a Landsat-like scale.

2.2. Data

2.2.1. Ground measurements

The EC systems provided measurement of turbulent fluxes at a frequency of 10 Hz in the midstream region of the Heihe River from 1 June to 14 September in 2012. Daily ET data were calculated using continuous 30-min flux data. To obtain continuous daily ET data, nonlinear regression was used to determine the relationship between latent heat flux (LE) and net radiation (R_n), and to fill the gaps of the flux data (Berbigier et al., 2001). On the rare occasions when there was a loss of > 50% of 30-min of data in one day, the daily ET of that day was considered missing, and the gaps were filled based on the relationship between daily averaged LE and R_n (Liu et al., 2013). Appendix A.1 provides more details about the measurements and data processing.

The following meteorological data were collected from the 21 AWSs installed at the LEA: wind speed and direction, air temperature, humidity, atmospheric pressure, precipitation, soil temperature, moisture profiles, net radiation, and soil heat flux. All meteorological data were measured at 10-min intervals. Appendix A.1 provides further details about the acquisition of net radiation and soil heat flux.

The irrigation water volumes of each irrigation district were monitored using flow meters at the entrances and exits of the main canals, subcanals, and field ditches in the midstream of the HRB (Ge et al., 2013; Wu et al., 2015). Groundwater pumping was also metered in each irrigation district. Surface irrigation water and remotely sensed ET data were used to evaluate irrigation water efficiency.

Table 1

Terra MODIS and Landsat 7 ETM+ data (April to October 2012) that were used in this study.

| Data type | MODIS (horizontal 25, vertical 05) | | | Landsat 7 ETM+ (path 133, row 33) | |
|-------------------|------------------------------------|------------------------|-----------------|---|---|
| | Reflectance (MOD09GA; MOD09GQ) | Albedo (MCD43B3) | LST (MOD11A1) | Visible and near infrared/shortwave infrared (VNIR/SWIR) | Thermal infrared |
| Resolution | 250–500 m | 1000 m | 1000 m | 30 m | 60 m |
| Day of year (DOY) | 092–305 (daily) | 092–305 (every 8 days) | 092–305 (daily) | 96 112 176 192 224 240 256 272 288 304 | 96 112 176 192 224 240 256 272 288 304 |

In addition to the data from these stations, in-situ measurements of crop height, canopy fractional vegetation cover (FVC), and leaf area index (LAI) were measured on various dates during the crops growth seasons.

2.2.2. Satellite data

Multi-source remote sensing data that had different spatial and temporal resolutions were from Terra MODIS and Landsat 7 ETM+ (Table 1). MODIS data were from the Land Processes Distributed Active Archive Center (LP DAAC) (<http://glovis.usgs.gov/>). Ten predominantly clear scenes of ETM+ were obtained from the United States Geological Survey (USGS) (<https://landsat.usgs.gov/>) for the period of April to October 2012 (day of year [DOY] 96, 112, 176, 192, 224, 240, 256, 272, 288, 304). These data were calibrated and atmospherically corrected for the shortwave reflectance band using the QUAC module (Bernstein et al., 2012) of the ENVI and for the thermal band using the Atmospheric Correction Parameter Calculator (Barsi et al., 2005) of NASA (<https://atmcorr.gsfc.nasa.gov/>).

The input parameters for the ET models (LST, normalized difference vegetation index [NDVI], FVC, LAI, emissivity, and canopy height and building height [HCHB]) had spatial resolutions of 100 m were derived from the MODIS and ETM+ products. The MODIS data, including land surface reflectance and TIR data, were processed to a daily scale at a spatial resolution of 100 m by fusing with the ETM+ data (Table 1). Appendix A.2 provides detailed descriptions of the image processing and data preparation procedures.

In addition, the following ET products were used for comparisons: MOD16 (every 8 days, 1000 m resolution; <http://www.ntsg.umt.edu/project/modis/mod16.php>) (Mu et al., 2011), ETWatch (Monthly, 1000 m resolution; <http://westdc.westgis.ac.cn/data/a07b59d3-61b1-463c-a2a3-8529c99e3a3c>) (Wu et al., 2012), ETMonitor (every 8 days, 250 m resolution; <http://westdc.westgis.ac.cn/data/dc02091c-773b-4cf4-92a2-ed8876e71be3>) (Jia et al., 2014), and Daily ET Datasets (2012) (daily, 1000 m resolution; <http://westdc.westgis.ac.cn/data/011ac821-ae1c-4061-a296-791695931ba2>) (Zhou et al., 2014).

2.2.3. Meteorological forcing data

To estimate surface fluxes at high spatiotemporal resolution in the study area, spatially explicit meteorological variables at the reference height (wind speed, air temperature, relative humidity, atmospheric pressure, and downward short-wave radiation flux) are needed. Thus, hourly near-surface meteorological forcing data (5 km resolution) produced by the Weather Research and Forecasting (WRF) model were used (Pan et al., 2012; Pan and Li, 2013). These data were interpolated using the bilinear resampling method, and averaged to determine daily values for all meteorological variables. Then, the WRF-derived

meteorological variables were downscaled to a spatial resolution of 100 m using regression-kriging (RK) (Redelsperger et al., 2006; Kang et al., 2015). The four steps of this procedure were: extracting numerical values from the observations and WRF data; fitting a linear regression model to the observations and the WRF outputs using the extracted numerical values; correcting the WRF data, based on the regression relationship, to remove potential biases; and interpolating the corrected WRF data from a spatial resolution of 5 km to 100 m using ordinary kriging. The precipitation volume during the growth period was determined from hourly precipitation data (Pan et al., 2012).

2.3. Auxiliary data

Land use/land cover (LULC) data were needed to specify surface roughness parameters and vegetation properties for the remote sensing based ET model (Ma et al., 2015). LULC data (100 m resolution) for the Zhangye region in 2005 were obtained from Yan (2011), and were updated based on the 2012 Landsat ETM+ data and a field survey (Liu and Bo, 2015). A high-resolution digital elevation model (DEM), obtained from NASA Shuttle Radar Topography Mission (SRTM, <http://srtm.csi.cgiar.org/>), was used to adjust the temperature of the in-situ measurements to sea level temperature (McVicar et al., 2007).

3. Methods

3.1. Estimation of High-Temporal and Landsat-Like (HiTLL) ET

Three cases of estimating ET at high temporal (daily) and Landsat-like spatial resolution (100 m resolution) (HiTLL) are described below (Fig. 2). **Case I** is for clear-sky days, when satellite remote sensing data at coarse (MODIS) and fine (Landsat-level data, ETM+) spatial resolutions are both available. In this situation, Landsat data were used to directly estimate instantaneous ET using the revised SEBS model (see Section 3.1.1), and then instantaneous ET estimates were upscaled to daily values using the constant solar radiation ratio (SolRad) method (Jackson et al., 1983). **Case II** is for clear-sky days, when only MODIS data are available. First, the high spatial and temporal resolution model input parameters were obtained using ESTARFM (Zhu et al., 2010; Yang et al., 2016). Then, the revised SEBS model, combined with the SolRad method, was used to estimate the daily ET from the fused data. **Case III** is for cloudy days, when both MODIS and ETM+ data are unavailable. For this condition, daily ET maps were estimated using a temporal reconstruction method, the reference evapotranspiration method (ET_{ET₀F}) (Xu et al., 2015). The fraction of reference evapotranspiration (ET_{ET₀F}), defined as the ratio of actual ET to reference ET (ET₀) from the FAO-56 method, was determined from data on all clear sky days.

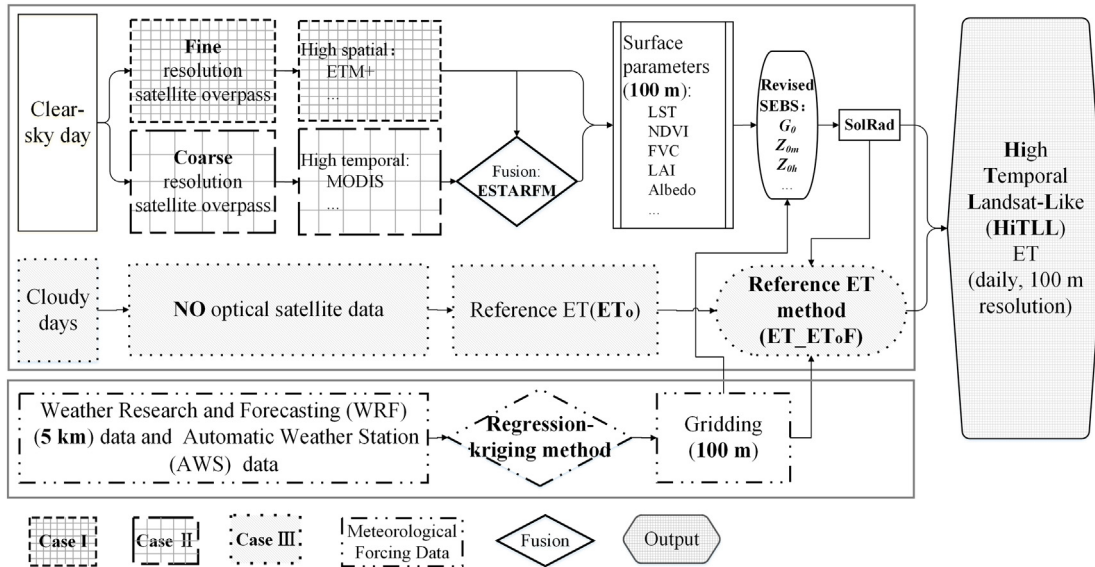


Fig. 2. Schematic diagram of estimating high temporal (daily) and Landsat-like spatial resolution (100 m resolution) (HiTLL) ET using remotely sensed data from MODIS and Landsat ETM +.

This method assumes that the ET₀F changes linearly between the two nearby clear-sky days. Thus, the cloudy-day ET₀F can be linearly interpolated using the clear-sky-day ET₀F. On cloudy days, daily ET can be obtained using the ET₀ and the interpolated ET₀F.

3.1.1. Modifications to the SEBS model

The SEBS model (Su, 2002) was used to estimate turbulent heat fluxes from satellite remote sensing data. This model has three components: computation of land surface physical parameters; calculation of surface roughness length for momentum transfer (z_{0m}) and heat transfer (z_{0h}); and estimation of the evaporative fraction (EF) based on the energy balance under limiting cases. The land parameters (derived from remote sensing) and regional meteorological data (herein, derived from the WRF using the RK) were used as model inputs, and the sensible heat flux (H) was computed using the Monin-Obukhov similarity theory (MOST) (Appendix B.1). The instantaneous LE or ET is then estimated as the difference between R_n and the sum of the calculated H and surface soil heat flux (G_0), assuming energy balance closure.

The SEBS model includes many land surface physical parameters, some of which have high uncertainty due to surface heterogeneity and scaling effects (Liou et al., 1998; Gao and Long, 2008; Tang et al., 2011). Thus, a sensitivity analysis for the critical model parameters (van der Kwast et al., 2009) was performed using the random-sampling high-dimensional model representation (RS-HDMR) approach (Ziehn and Tomlin, 2009). This approach uses a set of tools with variance-based analysis to capture the input-output relationship of complex models with many input variables. The results indicated that R_n, G_0 , z_{0m} , z_{0h} , and LST had the most impact on surface energy fluxes in the SEBS model. The current retrieval error of LST was approximately 1 to 2 K, leaving limited room for improvement, and the estimated R_n agreed with the measured values. Therefore, the parameterization schemes of G_0 , z_{0m} , and z_{0h} improve model predictions.

The G_0 was estimated as a fraction (Γ) of R_n in SEBS (Su, 2002). In the present study, we assumed G_0 increases with soil temperature (Tangney et al., 2012), and Γ was estimated as a function of the Temperature-Vegetation Dryness Index (TVDI) (Sandholt et al., 2002):

$$\Gamma = [\Gamma_c + (\Gamma_s - \Gamma_c)TVDI] \quad (1)$$

where Γ_s is 0.315 for bare soil (Kustas and Daughtry, 1990) and Γ_c is 0.05 for a full canopy (Monteith, 1973).

Based on the work of Zhang et al. (2004), an experimentally

determined model converting the equivalent geometric roughness length (η) to the surface roughness length for momentum transfer (z_{0m}) was used:

$$\ln(z_{0m}) = \xi \ln(\eta) + \xi_0 \quad (2)$$

$$\eta = \frac{\sum_{x=0}^{\Omega} \sum_{y=0}^{200} HCHB(x,y) \left(\frac{1}{D(x,y)} \right)^{2.5} \left(\frac{|dT(x,y)|}{LST(x,y)} \right)^{0.5}}{\sum_{x=0}^{\Omega} \sum_{y=0}^{200} \left(\frac{1}{D(x,y)} \right)^{2.5} \left(\frac{|dT(x,y)|}{LST(x,y)} \right)^{0.5}} \quad (3)$$

where η is the equivalent geometric roughness for a specific pixel, ξ and ξ_0 are model transformation factors, x and y define the location of the pixel, Ω is the fetch area of z_{0m} (Fig. A1 in Appendix B.2), HCHB is the canopy height or building height at the pixel (details in Appendix A.2), $D(x, y)$ is the distance between a given point and the measured point, and $dt(x, y)$ is the difference between the air temperature at the reference height and the LST. The value "200" represents the length (200 m) along the two straight border lines in the y -direction (Fig. A1 in Appendix B.2). The relationship between z_{0m} and η was determined by using measurements from the HiWATER-MUSOEXE. The calibrated model transformation factors were 0.39 (ξ) and -0.76 (ξ_0). The overall correlation coefficient (R) was 0.89 between $\ln(z_{0m})$ and $\ln(\eta)$ for residential areas, corn crops, orchards, wetland surfaces, and other areas.

The results of multiple parameterization methods for z_{0h} were compared to identify the best method for each land surface type (Li et al., 2017), due to high heterogeneity of the land surfaces in the study area. The difference between z_{0m} and z_{0h} can be described as a dimensionless heat transfer coefficient, $kB^{-1} = \ln(z_{0m}/z_{0h})$. The term kB^{-1} is highly sensitive to z_{0h} in the SEBS model, and different z_{0h} or kB^{-1} values will lead to large differences in heat flux estimates. To account for the effects of land surface heterogeneity on the estimation of heat fluxes, we needed to identify the most suitable z_{0h} or kB^{-1} parameterization scheme for each land cover type, thus we evaluated multiple schemes using measurements from EC towers on different types of land surfaces. In particular, the z_{0h} or kB^{-1} parameterization schemes in Yang et al. (2002), Kanda et al. (2007), Bosveld et al. (1999), and Su (2002) were assessed, and then the best parameterization method of z_{0h} or kB^{-1} for each land surface type was used for the SEBS model. Specifically, the schemes in Yang et al. (2002), Kanda et al. (2007) and Bosveld et al. (1999) were used for the bare soil, residential areas, and highly dense vegetation, respectively, and that in Su (2002)

Table 2

Statistical parameters of ET estimates for three different cases (1 June to 14 September 2012). Mean O: mean observed; mean P: mean predicted/modeled; MBE: mean bias error; MAPE: mean absolute percent error; RMSE: root mean square error; R: correlation coefficient.

| Item | Mean O | Mean P | y = ax | MBE | MAPE | RMSE | R |
|-------------------------------|--------|--------|-----------|--------|------|--------|------|
| | mm/day | mm/day | – | mm/day | % | mm/day | – |
| Case I | 4.86 | 4.87 | y = 0.96x | -0.20 | 10 | 0.78 | 0.90 |
| Case II | 5.10 | 4.89 | y = 0.95x | -0.14 | 12 | 0.83 | 0.83 |
| Case III | 3.89 | 3.63 | y = 0.95x | -0.14 | 14 | 0.82 | 0.83 |
| Case I, Case II, and Case III | 4.57 | 4.26 | y = 0.96x | -0.15 | 12 | 0.81 | 0.85 |

was employed for the interactions between vegetation and soil.

3.1.2. Spatial and temporal data fusion algorithm

STARFM and ESTARFM can capture spatial changes of reflectance from the cloud-free Landsat-like images (high resolution) by using two observed cloud-free MODIS-like images that were recorded on the same dates (i.e., two Landsat-MODIS pairs), and one additional MODIS-like image. In this procedure, these models first identify spectrally similar neighbor pixels, and then identify temporal changes from the cloud-free MODIS-like images (coarse resolution) to simulate images with high spatiotemporal resolution. Although STARFM and ESTARFM were originally designed to fuse the reflectance data from MODIS and Landsat to produce daily reflectance data, they can also be used to produce thermal maps at high spatiotemporal resolution (Weng et al., 2014). Recently, Yang et al. (2016) used the fusion method to predict LST data over heterogeneous areas. Moreover, based on the procedure for optimal algorithm blending proposed by Emelyanova et al. (2013) and Jarihani et al. (2014), our evaluation suggests that ESTARFM produced better high spatiotemporal resolution land surface reflectance and TIR radiance results from Landsat and MODIS data during the growth season of our study area. In this work, nine groups of ETM+ and MODIS images were used during the fusion process. Appendix B.3 provides the details of ESTARFM.

The high spatiotemporal resolution NDVI and albedo data were calculated by fusing the high spatiotemporal resolution data of the single-band reflectance of MODIS and ETM+, and the albedo maps were then gap-filled using the MCD43B3 product. Because heterogeneous radiance can be aggregated using the linear form (Weng et al., 2014), the TIR images were fused at the radiance level, and the fused radiance image was then converted to LST using Planck's law or the Stefan-Boltzmann law. Using ESTARFM, the IPFA was used to determine land surface physical parameters. This strategy differs from the ETFA proposed by Cammalleri et al. (2013, 2014a,b) and Semmens et al. (2016). Sections 4.2 and 5.2 provide comparisons of these strategies.

3.2. Assessment of irrigation water efficiency at multiple scales

Irrigation water efficiency during the growth season was calculated at the irrigation district and the village scales using the following equation from Ahadi et al. (2013):

$$f_{eff} = \frac{ET - P_e}{TIW} \quad (4)$$

where f_{eff} is the irrigation water efficiency, ET is the season-cumulative HiTLL ET (modeled using multisource remote sensing data during the growth period), P_e is the effective precipitation (calculated from the monthly precipitation data for each irrigation district), TIW is the total irrigation water during the growth period, and TIW is the sum of applied groundwater and surface water (Wu et al., 2015). According to Ahadi et al. (2013), if the total monthly rainfall is < 1.85 mm/month, the value of P_e should be set to 0.

3.3. EC footprint model for validation of satellite-based ET

Due to the spatial mismatch between the EC footprint and the spatial resolution of satellite-based ET in this study, an EC footprint model is needed. The flux footprint can be used to describe the contribution of an area to flux measurements, based on the source area and footprint weights. Jia et al. (2012) and Bai et al. (2015) reported the use of satellite pixels within the EC flux source area as validation pixels. Although the EC source area may include many satellite pixels, satellite-based ET at the EC source area was estimated by summing the footprint-weighted ET at the validation pixels. Thus, to estimate the flux footprint of the EC measurements, an Eulerian analytic flux footprint model was implemented, and the flux contribution of the source area was set to 90%, as proposed by Kormann and Meixner (2001).

4. Results

4.1. Validation of the estimation scheme for HiTLL ET

The validation results indicated that the three cases of HiTLL ET reliably reproduced the daily ET over different oasis surfaces in the midstream of the HRB from 1 June to 14 September in 2012 (mean MAPE: 12%, mean RMSE: 0.81 mm/day, mean R: 0.85) (Table 2). We integrated daily ET estimates at a Landsat-like scale (100 m resolution) to the same spatial representation of the EC system using the footprint model, and compared the integrated ET estimates with EC measurements from the flux observation matrix (18 stations) in the HiWATER-MUSOEXE for the three different cases (Fig. 3a; Table 2). The results show good agreement between the daily estimated ET and EC values (Fig. 3a). More specifically, the best estimates were from the high-resolution remote sensing data (Case I); the second-best were from the coarse-resolution data, with high-resolution data obtained using the fusion algorithm (Case II); and the third-best were from the gap-filling method (Case III).

Comparison of the observed and estimated daily ET for the different land cover types indicated that ET estimates for maize, orchards, and vegetables had the best accuracy based on MAPE, followed by wetlands and villages (Fig. 3b and Table 3). The largest MAPE (29%) of estimated ET for the residential (villages) site is likely due to its high surface heterogeneity (Jia et al., 2012; Song et al., 2016), which consists of residences, roads, and cropland, and because scale mismatch may cause large errors. The second-largest MAPE (21%) and largest RMSE (1.13 mm/day) was for wetlands (Fig. 3b), possibly due to the presence of mixed pixels of water and reeds. Because the surface temperature of wetlands is a function of the temperatures of the large coverage of water and the small coverage of reeds, this could cause large estimation errors, and even systematic bias, in the estimated ET. The magnitude of the error (MBE) was very similar for orchards (-0.66 mm/day) and wetlands (0.64 mm/day), although the ET was underestimated for orchards but overestimated for wetlands. Analysis of the relationship of ET residual error (estimated ET – observed ET) with environmental factors indicated that volumetric water content (VWC) and LST had strong correlations with ET residual error (details in Appendix C.1).

Comparison of observed daily ET time series and estimated ET

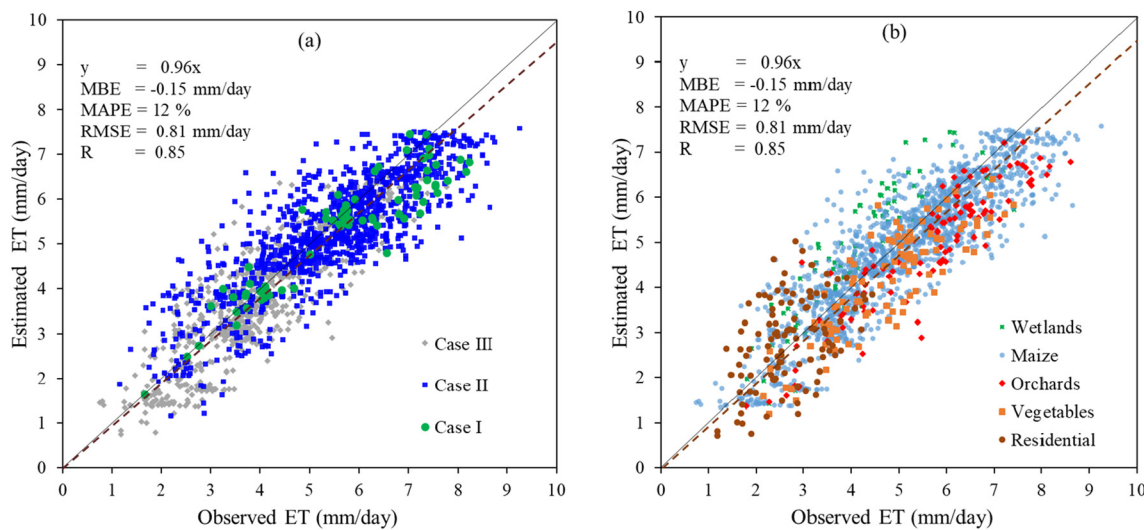


Fig. 3. Comparison of EC measurements and daily ET estimates at a Landsat-like scale for (a) three different cases (Case I: 5 days, Case II: 61 days, Case III: 40 days) and (b) five different land cover types (1 June to 14 September 2012).

during the growth season showed that the modified SEBS model successfully reproduced daily ET at sites #1 (vegetables) (Fig. 4a), #15 (maize) (Fig. 4b), and #17 (orchards) (Fig. 4c). Overall, the temporal variations of the estimated and observed ET values were similar during the growth season, especially during the middle of this season; however, there were larger discrepancies during the early and late stages of the growth season, and during periods with precipitation. Specifically, early in the growth season (DOY92 [01 Apr] to DOY152 [31 May]), the surface heterogeneity of the three sites gradually increased due to the co-occurrence of young crop plants and bare soil. There were also spatial variations (surface heterogeneity) during flood irrigation events at different times. Late in the growth season (after DOY256 [12 Sept]), the trends of ET over the three sites were similar, but the amplitudes differed. This is because the heterogeneity of the surfaces at the three sites increased due to co-occurrence of bare soil with frost-withered maize. The notable trough in the HiTLL ET during the peak of the growth period (DOY197 [15 July] to DOY212 [30 July]) in the oasis (gray-shaded areas in Fig. 4) could be due to the small decrease in shortwave radiation because of the cloudy conditions at that time. In addition, Fig. 4 also shows a general consistency between the seasonal variations of LAI and ET. Overall, the estimation scheme of HiTLL ET characterizes changes of ET following rainfall and irrigation, which are indicative of changes in crop growth and phenology that cannot be characterized by Landsat data.

We also compared the HiTLL ET with existing remote sensing ET products for the oasis ($30 \text{ km} \times 30 \text{ km}$) in the midstream of the HRB (Fig. 5). Despite some differences, these ET products had similar seasonal variations. More importantly, the comparisons show the advantage of the HiTLL ET over other ET products in characterization of the fine-spatiotemporal properties of different land cover types. For example, HiTLL ET indicated obvious differences in ET values over roads, villages, and croplands, and also showed differences between the

watercourses of the Heihe River and oasis areas during July and August, features not captured by other ET products.

The in-situ measurements have high spatial heterogeneity, but use of a high spatiotemporal resolution product, such as HiTLL ET, can eliminate some of the resulting uncertainties. The method of scaling the fine-resolution remote sensing information to validate the ET product at a coarse resolution might be effective (Anderson et al., 2008, 2011; Jia et al., 2012). There were significant differences in the magnitudes and spatial distributions of the monthly remotely sensed ET products (MOD16, ETMonitor, and ETWatch) and HiTLL ET (this study) over the LEA ($30 \text{ km} \times 30 \text{ km}$) in the midstream of the oasis of the Heihe River (Fig. A3). In particular, the MOD16 product produced lower estimates than the other products in the oasis areas, with a bias of approximately -50 to -100 mm/month ; the ETMonitor product overestimated ET by 10 to 20 mm/month during July and August; the ETWatch product had similar distributions as the MOD16 product during July and August, and a bias that ranged from -100 to -10 mm/month . The large discrepancies between these coarse-resolution ET products and the HiTLL ET suggest that these other ET products have highly biased estimates, and are therefore unsuitable for assessment of ET changes in regional areas. This further supports the need to produce HiTLL ET for regional assessments of ET variations.

4.2. IPFA versus ETFA

We compared the input parameter fusion approach (IPFA) with the ET fusion approach (ETFA) to identify the most suitable method for ET estimation in our study area. Most recent studies obtained estimated ET values at high spatiotemporal resolution by fusing MODIS- and Landsat-derived ET maps (Cammalleri et al., 2014a,b; Semmens et al., 2016; Bai et al., 2017). However, most ET estimation models were developed for simple and homogeneous surfaces (Hu and Islam, 1997), even though

Table 3

Statistical parameters of daily ET for different land cover types at a Landsat-like-scale (1 June to 14 September 2012). Abbreviations are the same as in Table 2.

| LULC | Mean O | Mean P | $y = ax$ | MBE | MAPE | RMSE | R |
|------------------------|--------|--------|-------------|--------|------|--------|------|
| | mm/day | mm/day | – | mm/day | % | mm/day | – |
| Maize | 5.02 | 4.92 | $y = 0.95x$ | -0.11 | 12 | 0.79 | 0.87 |
| Vegetables | 4.78 | 4.23 | $y = 0.88x$ | -0.55 | 14 | 0.85 | 0.85 |
| Orchards | 5.54 | 4.88 | $y = 0.88x$ | -0.66 | 13 | 0.90 | 0.91 |
| Wetlands | 4.30 | 4.93 | $y = 1.12x$ | 0.64 | 21 | 1.13 | 0.78 |
| Residential (villages) | 2.64 | 2.85 | $y = 1.05x$ | 0.21 | 29 | 0.95 | 0.44 |

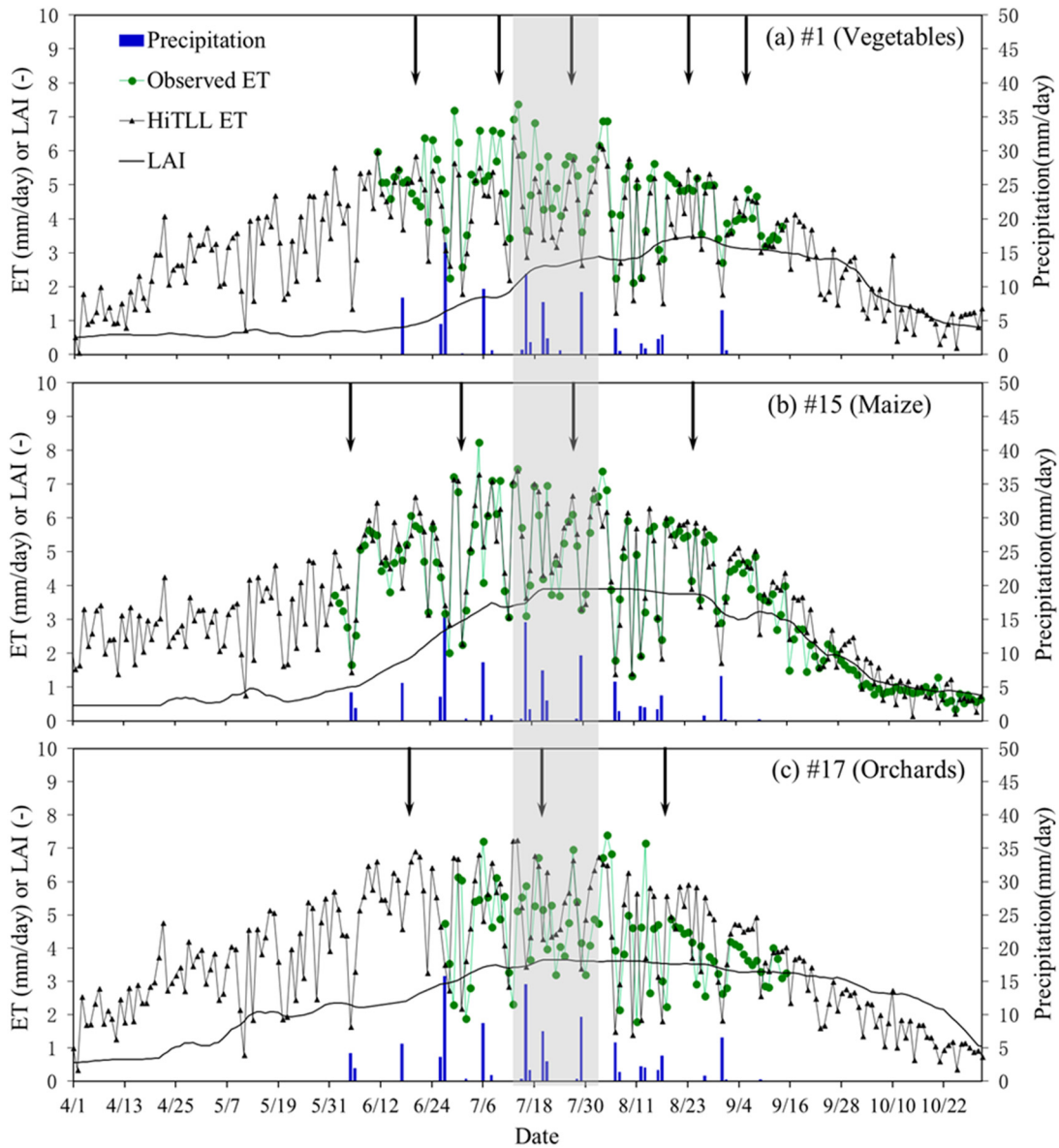


Fig. 4. Time series of observed daily ET (green circles), HiTLL ET (black triangles), and LAI (black line) for (a) Site #1 (vegetables), (b) Site #15 (maize), and (c) Site #17 (orchards) (1 April to 31 October 2012). Blue bars indicate precipitation events and arrows indicate irrigation dates. (For interpretation of the references to color in this figure legend, the reader is referred to the web version of this article.)

many natural land surfaces are heterogeneous. The failure of these models to consider this heterogeneity may lead to large errors in estimation of ET (Kustas et al., 2003; Tang et al., 2013; Peng et al., 2016). Thus, to evaluate the performance of these methods, we classified the surface into two categories for assessment of the accuracy of ET at fine spatiotemporal resolution: (i) a spatial heterogeneous surface with LAI values of 0.6 to 2.0 (i.e., before the crop is at full cover [10 July] and the end of the crop growth period [10 September]), or a mixed surface consisting of residential areas, roads, and cropland; and (ii) a spatial homogeneous surface with LAI values of 2.0 to 4.2 (i.e., during the crop growth period, and after closure of the crop canopy).

A comparison of the results indicates the IPFA was superior to the ETFA for spatially heterogeneous surfaces, although they had similar performances for homogeneous surfaces (Fig. 6). Specifically, the performance of the ETFA was a slightly poorer over the spatial heterogeneous surfaces. For example, on one highly heterogeneous surface (residential area, #4) which had buildings, roads, and crops, the ETFA generally overestimated ET and had larger bias errors than the IPFA. Consequently, the data processing and nonlinear retrieval models of ET

estimation produce similar results when the land surface is relatively homogeneous, but failure to consider spatial heterogeneity of the surface physical parameters and different landscapes within mixed pixels leads to a large bias.

4.3. Spatiotemporal variations of ET in irrigated agricultural areas

4.3.1. Variations of 10-day cumulative ET

The 10-day cumulative ET map based on the HiTLL ET (Fig. 7) shows the spatial distributions of ET varied from early April to late October in 2012. Overall, the ten-day ET had small variations early in the growth season (early April to late May), although there were slightly larger variations in the watercourses of the Heihe River. Analysis of the spatial variations (σ_{spat}) indicated the ten-day ET was more homogeneous during early April to late May (σ_{spat} : 3.4 mm) than during early June to late July (σ_{spat} : 7.2 mm). During the early growth season (early April to late June), the ET of the oasis area increased significantly; at the end of the growth season (late August to late September), the crops were mature, frost began to occur, and there were

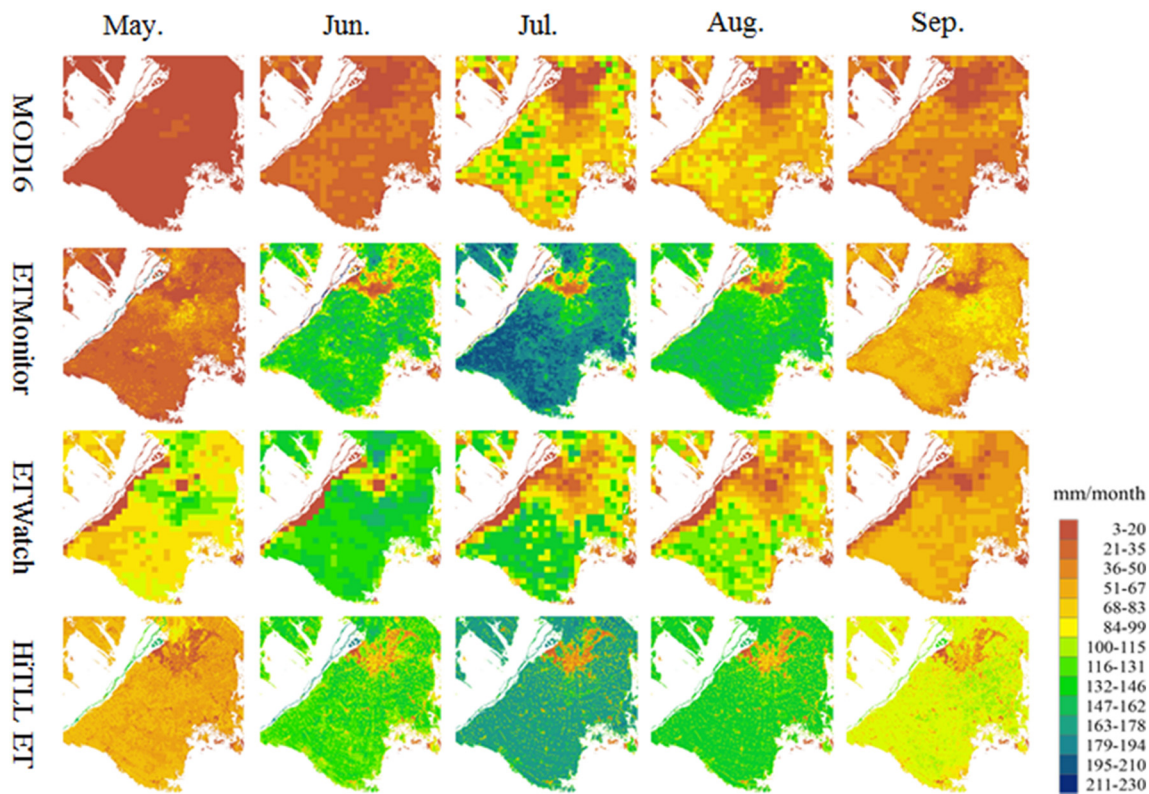


Fig. 5. Spatial distributions of monthly remotely sensed ET products over the oasis area (LEA, 30 km × 30 km) in the Heihe River (May to September 2012). Row 1: MOD16 (every 8 days, 1000 m resolution), Row 2: ETMonitor (every 8 days, 250 m resolution), Row 3: ETWatch (monthly, 1000 m resolution), Row 4: HiTLL ET (daily, 100 m resolution; this study).

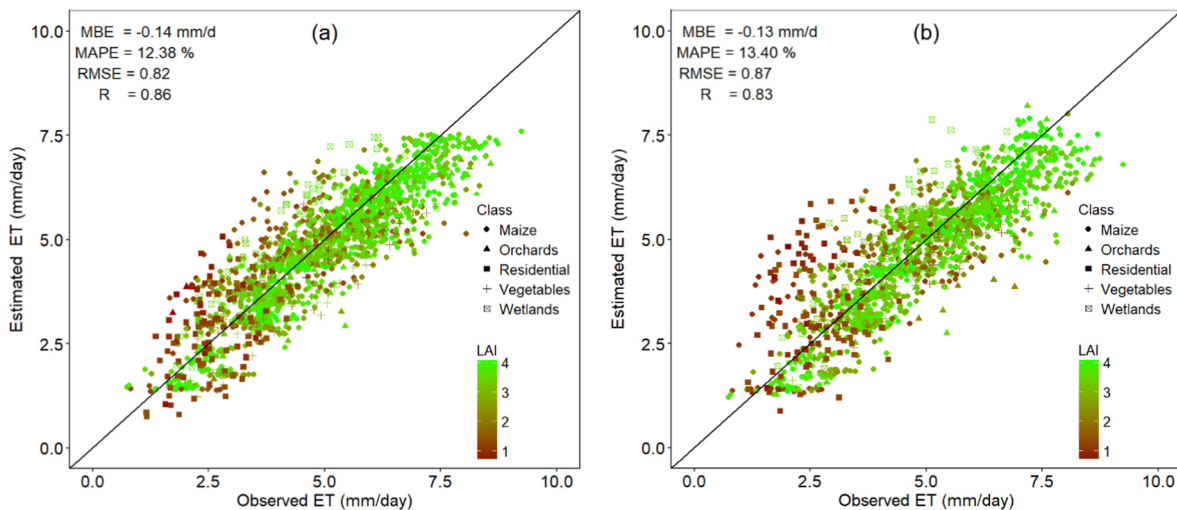


Fig. 6. Comparison of ET estimations using (a) IPFA and (b) ETFA (1 June to 14 September 2012).

notable decreases of ET by mid-September. Variations of ET during the growth period could be explained by differences in vegetation, phenology, irrigation practices, weather conditions, and field management (Yang et al., 2012).

4.3.2. Variations in season-cumulative ET

We also found differences in season-cumulative ET among the different land covers from April to October in 2012 (Table 4), although there were similar ET values in farmlands that had maize, barley, potatoes, orchards, and vegetables (560 to 640 mm). This is because flood irrigation at these sites led to soil moisture level that was nearly at field capacity. For example, site #15 had a VWC of approximately 20 to 40%

at a depth of 0 to 40 cm. These season-cumulative ET results are consistent with previous studies. In particular, Wu et al. (2015) reported that the ET of crops in the Zhangye oasis ranged from 360 to 680 mm from April to September, based on the SEBS model and the temporal gap-filling method. Zhao and Ji (2010) used a model (FAO-56-PM daily) calibrated with data from Linze (adjacent to our study area) and reported an estimated farmland ET of 671 mm during the growth season of 2009.

4.3.3. Variations in daily ET during irrigation events

Our HiTLL ET estimates were better in capturing subtle variations of ET caused by changes in the timing and extent of flood irrigation than

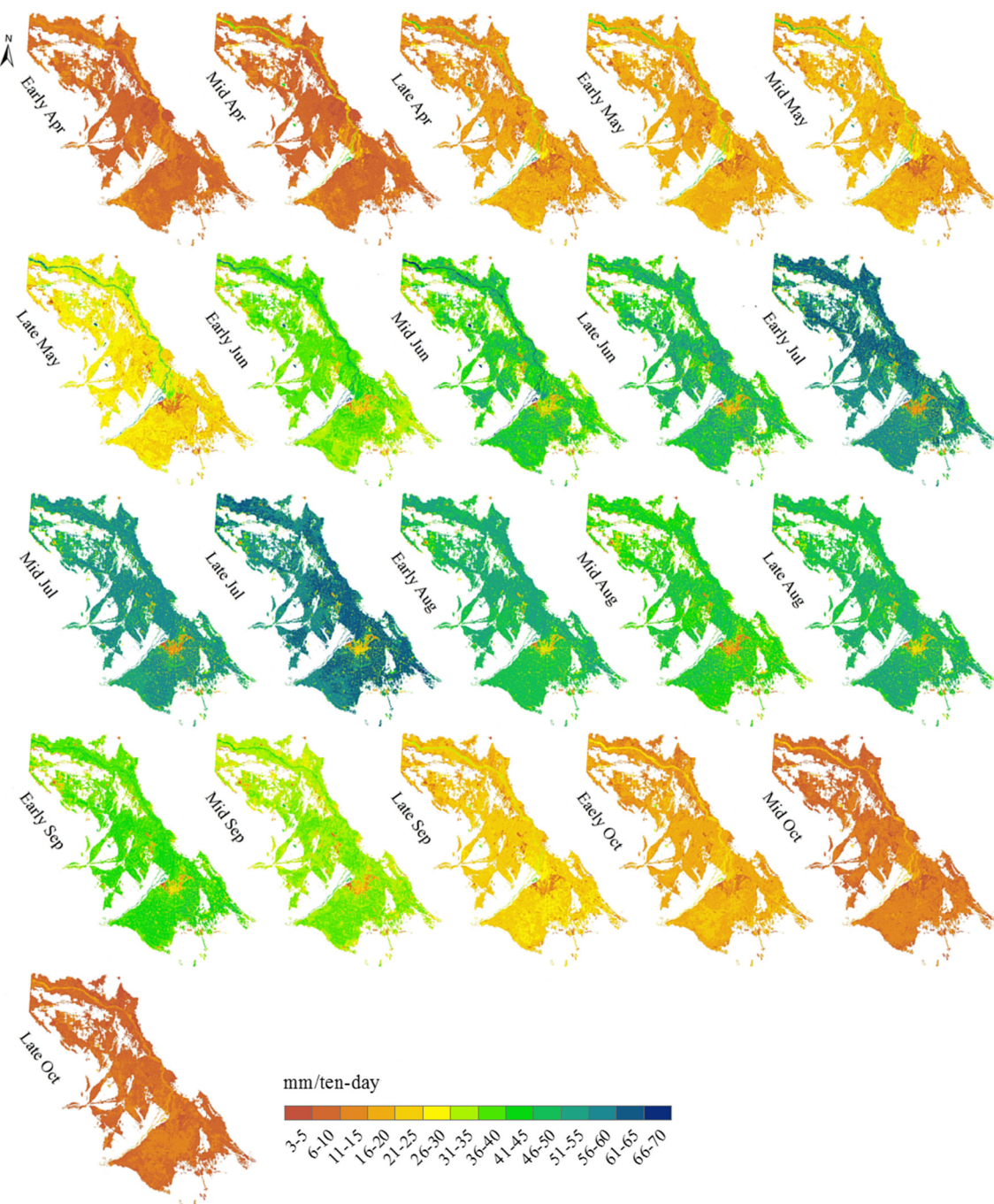


Fig. 7. Spatial variations of remotely sensed ET at 10-day intervals in the midstream of the oasis area (early April to late October 2012).

the coarse-resolution ET estimates (Fig. 8). The agricultural water demand of our study area is mainly met by flood irrigation from the nearby Heihe River, and there are typically 5 or 6 flood irrigation events in the oasis region during the growth season. According to the HiWATER-MUSOEXE experiment, when oasis farmland is not irrigated, the volumetric soil water content remains at 20 to 30% at depths of 0 to 40 cm; however, an irrigation event causes the volumetric soil water

content to rapidly increases to approximately 40%. Thus, irrigation increases soil moisture, and this leads to increased soil evaporation and vegetation transpiration, and increases the difference of ET between irrigated and non-irrigated farmlands. During the process of irrigation, spatial variations in ET develop in oasis areas, and these depend on the timing and extent of irrigation. Our HiTLL ET product successfully characterized these irrigation-induced spatial variations in ET (Fig. 8).

Table 4

Average ET for different LULC types over the oasis area ($90 \text{ km} \times 90 \text{ km}$) (April to October).

| LULC | Water bodies | Wetlands | Orchards | Maize | Barley | Vegetables | Potatoes | Residential (villages) |
|-----------------------------------|--------------|----------|----------|-------|--------|------------|----------|------------------------|
| Average season-cumulative ET (mm) | 853 | 715 | 637 | 625 | 603 | 589 | 563 | 319 |

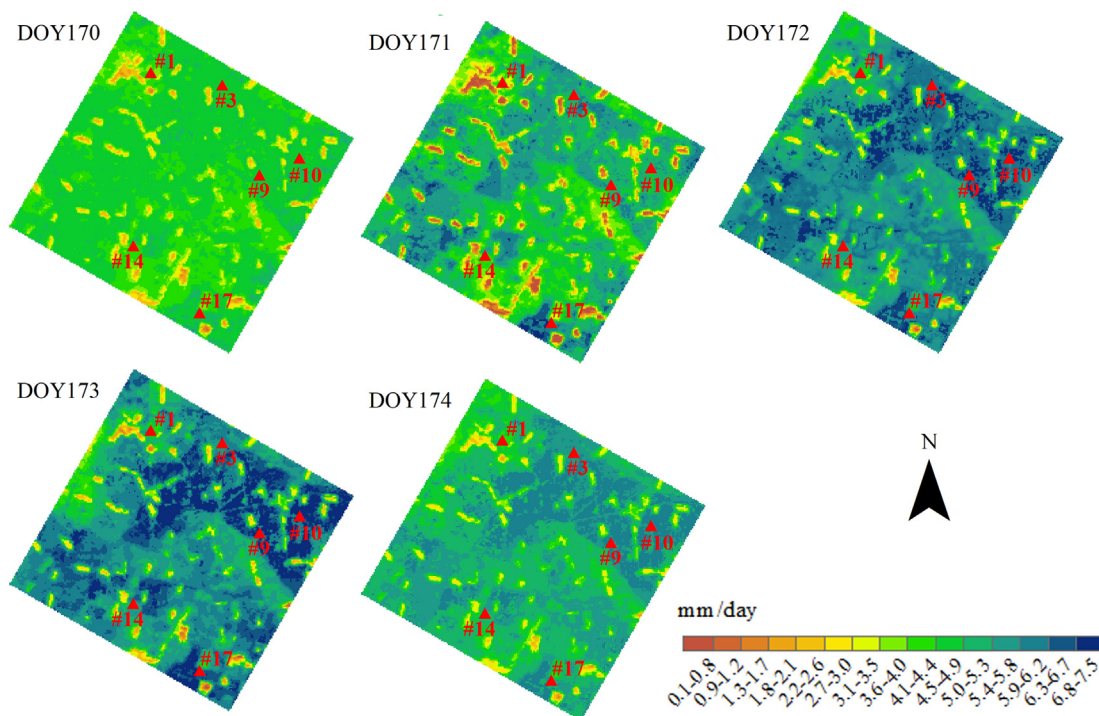


Fig. 8. Spatiotemporal variability of daily ET at a Landsat-like scale (100 m resolution) in the KEA ($5.5 \text{ km} \times 5.5 \text{ km}$) during an irrigation period (18 June [DOY170] to 22 June [DOY174] 2012).

For example, when irrigation began in the orchards (#17) on DOY 171 (19 June), in the vegetable fields (#1) on DOY 172 (20 June), and in the maize fields (#14) on DOY 173 (21 June) in the KEA, the HiTLL ET indicated rapid increases of ET in these sites. The HiTLL ET also characterized temporal changes in ET. For instance, the HiTLL ET shows one day increases of ET at maize fields in Site #3, Site #9, Site #10, and Site #14 due to irrigation (DOY170 vs. DOY171 and DOY172 vs. DOY173). On the other hand, the coarse-resolution ET products (MOD16, ET-Monitor, ETWatch, and Daily ET Datasets [2012]) did not capture the spatiotemporal variations in ET during the irrigation period (Fig. A4), so they cannot be used to improve irrigation water efficiency at local scales. This comparison clearly shows the advantages and necessity of producing a high spatiotemporal resolution product, such as HiTLL ET.

4.4. Assessment of irrigation water efficiency at multiple scales

We evaluated irrigation water efficiencies in the 12 irrigation districts during the growth season, at the level of the irrigation district and the village, in the midstream of the Heihe River (Fig. 9). The average irrigation water efficiency was 70%, meaning that ET accounted for

70% of the total irrigation water flowing into the 12 irrigation districts. The irrigation water efficiency in the Wujiang irrigation district was the highest (94%), followed by Pingchuan (88%) and Liaoquan (84%). The efficiencies of other irrigation districts ranged from 57% to 79%, and the lowest efficiencies were at the Yingke (57%), Shangsan (60%), and Liyuan rivers (62%). The average effective precipitation on farmland of the study area was approximately 106 mm from April to October, and the irrigation water depth was 690 mm. The irrigation water depths in the 12 irrigation districts ranged from 564 to 828 mm during the growth season, and the average ET over the oasis region was 587 mm.

Fig. 10 shows the irrigation water efficiencies at the village scale in the KEA ($5.5 \text{ km} \times 5.5 \text{ km}$). The KEA is located in the Yingke and Daman districts, and is representative of the 12 studied irrigation districts. In this KEA, the average ET of cropland was 625 mm and the average irrigation water efficiency in the 32 villages was 62%. However, the irrigation water efficiency varied significantly among the 32 villages. Specifically, in the northern part of the KEA, the irrigation water efficiency was 93% at Kangning (No. 9), 86% at Jincheng (No. 3), 70% at Shangtouzha (No. 4), and 71% at Shiqiao (No. 7) (Fig. 1, right); in contrast, in the southern part of the KEA, the efficiency was 44% at Xiaoman (No. 2), 47% at Wuxing (No. 4), and 55% at Zhonghua (No. 6) (Fig. 1, right). Overall, the irrigation water efficiency in the north was 10% higher than that in the south at the village scale in the KEA. There could be several reasons for these results. First, soil in the northern part of the KEA contains slightly more silt and clay in the northern part of the KEA, and this prevents excessive percolation of irrigation water, and thereby provides adequate soil water for ET. Another reason may be that the irrigation exceeded ET demand by > 50% in the southern part of the KEA. In particular, the irrigation depth was 1229 mm at Xiaoman (No. 2) but the ET demand was 650 mm. These results indicate that irrigation water should be monitored more carefully and allocated more rationally to improve irrigation water efficiency at the field scale in this region.

The disparate irrigation water efficiencies among the 12 irrigation districts and 32 villages reflect strong spatial heterogeneity in ET and irrigation in our study area, and strongly support the necessity of

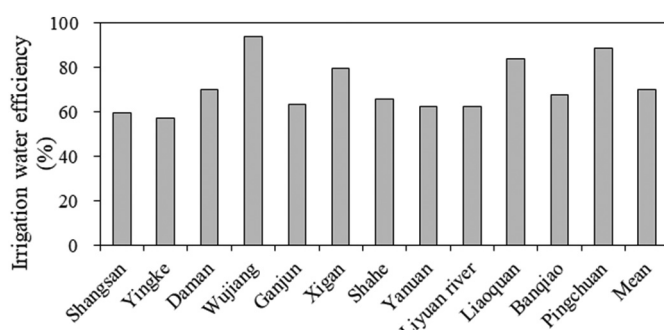


Fig. 9. Irrigation water efficiencies of the 12 irrigation districts in the midstream of the Heihe River during the plant growth period (2012).

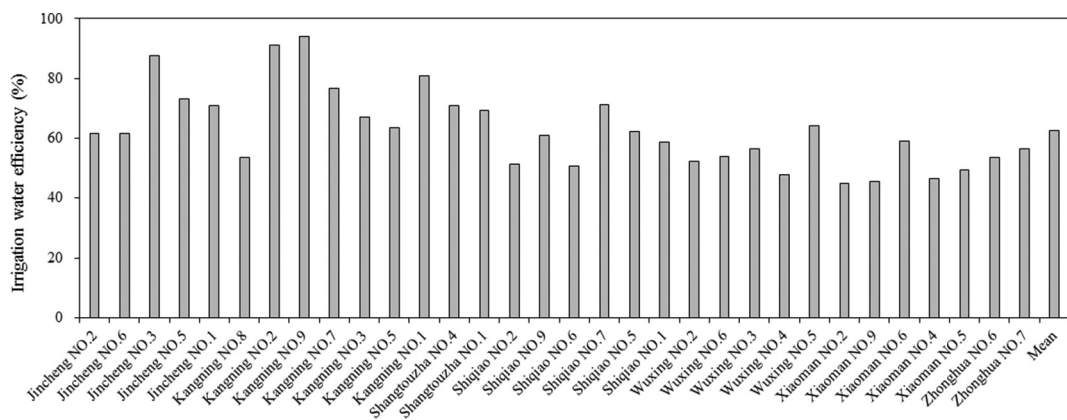


Fig. 10. Irrigation water efficiencies of the 32 villages in the KEA ($5.5 \text{ km} \times 5.5 \text{ km}$) during the plant growth period (2012).

calculating ET at a high spatiotemporal resolution. In light of the large heterogeneity of other irrigated areas throughout the world, such as the Colorado River Basin (Senay et al., 2016) and the Yellow River Basin (Bai et al., 2017), further efforts are needed to produce high resolution ET data so that irrigation water efficiency can be improved at local scales. These efforts could help to mitigate water scarcity in many regions of the world.

5. Discussion

5.1. Uncertainties in HiTLL ET estimation

Our results indicate that the HiTLL ET scheme can provide accurate regional ET estimates at a high spatiotemporal resolution. Fusing land surface reflectance and TIR radiance data from MODIS and Landsat using the ESTARFM provides estimates of ET at the field scale. Nonetheless, the uncertainties associated with the use of meteorological forcing data and remote sensing data could affect the outcome of this procedure. For example, at site #1, the HiTLL ET was underestimated during the middle of the growth season (DOY 180 to 200). Furthermore, comparison of the results of Case I, Case II, and Case III indicated that the gap-filling ET data (Case III) were less accurate. The linear interpolation of clear-sky ET values to continuous daily ET for determination of ET_o may have led to errors because crop growth does not necessarily conform to this simple linear rule. In addition, precipitation or irrigation events between two clear-sky days will alleviate soil moisture stress, but this change in soil moisture will not be captured by the ratio of actual ET to ET_o (Xu et al., 2015). Alfieri et al. (2017) suggested that temporal reconstruction has limited use, and a return interval of no > 5 days is necessary for accurate daily ET estimates, and that significant errors may occur if the gap size is large. Therefore, the fusion of retrieved LSTs with satellite passive microwave remote sensing data may improve ET estimations in cloudy regions (Zhou et al., 2015; Duan et al., 2017). Besides, comparison of our observations indicated that ET was slightly underestimated for maize (-0.11 mm/day), vegetables (-0.55 mm/day), and orchards (-0.66 mm/day), and slightly overestimated for wetlands (0.64 mm/day) and residential sites (0.21 mm/day). This may be due to inappropriate model assumptions (Timmermans et al., 2013), uncertainties associated with model inputs and parameterizations (Kustas et al., 2016) or EC measurements (Cheng et al., 2017), time upscaling (Van Niel et al., 2011, 2012; Ryu et al., 2012; Cammalleri et al., 2014a,b), or a mismatch in the spatial scales between estimated ET and EC measurements (Jia et al., 2012). Further, during periods of rain, most of the poor EC measurements were replaced by the gap-filled ET, and this may have increased the bias in the ET estimates.

The ground measurements from the EC towers and the AWS system have inherent uncertainties (Wang et al., 2015; Cheng et al., 2017) that

will impact the HiTLL ET product. For example, there were very large EC values at Site #1 (vegetables) on DOY 181, DOY187, DOY190 and DOY196. The extremely high values of measured ET at this site, which has well-irrigated fields covered by vegetables, may be due to strong local horizontal advection of dry and warm air from adjacent residential areas due to windy conditions following irrigation events (Cammalleri et al., 2014a,b; Xu et al., 2017).

We observed a systematic overestimation of ET when there was very low surface soil moisture, high radiative energy, and high atmospheric water demand (Fig. A2a, b, and d). This was also previously reported by Gu et al. (2006) and Mallick et al. (2014, 2015) in other arid and semi-arid regions. Furthermore, the relationships among VWC, Rn, atmospheric vapor pressure deficit [VPD], dT, and LAI are dynamic, in that variations of one factor can lead to variations in other factors (Gu et al., 2006). For instance, our residual error analysis indicated that higher errors in ET estimation occurred with higher dT ($> 2 \text{ K}$; Fig. A2d and e), emphasizing the challenge of estimating ET under conditions of large atmospheric water demand ($> 20 \text{ hPa}$) and low wind speed ($< 2 \text{ m/s}$). The dT might have a large effect under conditions of mixed landscapes within pixels ($\text{LAI} < 2.5$), because a large amount of mixing contributes to the uncertainty of ET estimations. These may also explain our observation of higher MAPE values over heterogeneous surfaces, such as residential areas.

5.2. IPFA versus ETFA

The estimated daily ET data at a Landsat-like scale (100 m resolution), using IPFA and based on high-resolution inputs at 100 m, provided a satisfactory characterization of the heterogeneous landscape surface. In particular, LST sharpening improved the descriptions of heterogeneous surfaces, based on the thermodynamically driven force of turbulent heat flux. In this case, the estimated ET considered the different parameterization schemes of subpixel landscapes, thus improving their accuracy (Fig. 6a). Furthermore, the IPFA effectively decreased the scale errors that result from heterogeneity, because the 250 to 500 m VNIR, the 1000 m TIRS of MODIS, the 30 m VNIR, and the 60 m TIRS of the ETM + data were fully used. In other words, the IPFA accounted for the effects of mixed pixels. In contrast, ET estimates at 1000 m obtained from ETFA do not present surface details in the mixed pixels, and do not consider multiple parameterization methods in subpixel landscapes (Peng et al., 2016; X.J. Li et al., 2017).

For more homogeneous surfaces, there were only small differences in daily average ET between the IPFA and ETFA (within 0.1 mm/day ; Fig. 6a, b; $\text{LAI} > 2.0$); however, when the LAI was > 3.5 , the IPFA had a slightly poorer performance. Jarihani et al. (2014) reported that the “Index-then-Blend” (IB) approach produced more accurate vegetation indexes when using satellite remote sensing data. Thus, future studies may be able to reduce the uncertainty of the input parameters (e.g.,

NDVI) that have high spatiotemporal resolution by using an IB approach. Although the IPFA provides a better description of surface heterogeneity than the ETFA, it is more computationally expensive because it fuses multiple bands, rather than using the immediate ET results.

5.3. Spatial and temporal data fusion algorithm

The growing interest in the spatial dynamics of water use at regional scales has led to increased use of satellite remote sensing data to map ET (Kalma et al., 2008). Data fusion methods that use remote sensing data from multiple sources (i.e., MODIS and ETM+), some at high temporal resolution and some at high temporal resolution, allows estimation of ET at high spatiotemporal resolution (Cammalleri et al., 2013, 2014a,b; Semmens et al., 2016). The daily ET estimates in the present study yielded a MAPE of 12% and an RMSE of 0.81 mm/day, similar to previous studies. For example, Cammalleri et al. (2013) reported RMSE values of ~0.5 to 1.0 mm/day at the field scale in irrigated agricultural areas.

However, it should be noted that ESTARFM fusion method has several limitations. One limitation is that remote sensing parameters (e.g., orbit parameters, bandwidth, acquisition time, and spectral response function) acquired from different satellite sensors on the same date may not provide comparable data. This method also does not consider differences in the overpass times of the Landsat and MODIS sensors. Although the near-nadir viewing and solar geometries of MODIS are similar to those of Landsat (Gao et al., 2006), they have different overpass times due to their different orbital parameters. Furthermore, the original ESTARFM could be improved to better predict LST data by considering the diurnal temperature cycle (Zhou et al., 2013; Quan et al., 2018). A second limitation of ESTARFM is that it uses a linear model to predict changes in surface reflectance and TIR bands, and this may lead to inaccurate characterization of the underlying dynamics. Therefore, combining ESTARFM with a non-linear model (Weng et al., 2014) or use of an unmixing-based algorithm (Gevaert and García-Haro, 2015) could improve the results.

5.4. Assessment of irrigation water efficiency at multiple scales

We assessed irrigation water efficiencies at the scales of irrigation districts and villages. The results show that the mean irrigation water efficiency was 70% in the 12 irrigation districts in the midstream region of the HRB, but was 62% in the 32 villages in the KEA. Within the river basin, switching scales can change the apparent irrigation water efficiency from poor to good, because water initially regarded as ‘wasted’ is reclassified as ‘reused’ (van Halsema and Vincent, 2012). In other words, irrigation water that was considered wasted at the village scale may be considered reused at the irrigation district scale. This is because some of the flood irrigation water remains in the surface soil after irrigation, and approximately 35% of the irrigation and rain water is lost to the soil layer below 80 cm. This loss occurs because surface water rapidly infiltrates the soil after irrigation or heavy rain, and cannot be used by crops (Wen et al., 2016). The irrigation water lost to the root zone layer could therefore increase the amount of groundwater discharge (baseflow), and may benefit other districts if it is reused by crops or shelterbelts. This reallocation of irrigation water could account for

the lower localized irrigation water efficiency at the village scale than at the irrigation district scale in the midstream of the HRB. Therefore, irrigation water efficiency is greater at larger scales. Other factors could also influence irrigation water efficiency (van Halsema and Vincent, 2012; Ahadi et al., 2013; Li et al., 2018). For example, in the midstream of the HRB, a large amount of irrigation water recharges the groundwater and is then pumped out for irrigation, indicating frequent exchanges between the surface water and groundwater. We also found that different land covers had different water consumptions, although these differences were small. The results of the present study highlight that fine-scale monitoring and control of irrigation water is necessary for effective management of water resources within a river basin.

6. Conclusion

Accurate and high spatiotemporal resolution ET products, which can be derived from satellite data, are required for quantification and improvement of irrigation water efficiency, but there are trade-offs between the spatial and temporal resolutions of satellite data. This study showcased our efforts to overcome this limitation by use of multi-source remote sensing data fusion, and also demonstrated the merits of the high spatiotemporal resolution ET product in quantifying irrigation water efficiency at high resolution for an arid irrigation area in the Heihe River Basin (HRB) of Northwest China. Our validation results indicated that the HiTLL ET estimation scheme effectively predicted continuous daily ET at a Landsat-like scale (100 m resolution) on clear-sky days. Additionally, our proposed IPFA performed better than ETFA for land surfaces with high spatial heterogeneity. The seasonal variations and spatial patterns of the HiTLL ET tend to be realistic, and they indicate subtle variations among roads, villages, river courses, and farmland. Furthermore, our estimation of irrigation water efficiency from the high spatiotemporal resolution ET dataset indicated that efficiency differs at the scale of the irrigation district (70%) and the village (62%). This underscores the need to estimate ET at a high spatiotemporal resolution to guide irrigation water management decisions at the locally fine scale (e.g., at the village scale).

The HiTLL ET estimation scheme proposed in this study could also be used to monitor agriculture water consumption and quantify irrigation water efficiency at field scale in other arid and semi-arid irrigated areas. Future work will focus on fusing retrieved LSTs with satellite passive microwave remote sensing data to improve the accuracy of the HiTLL ET estimations on cloudy days.

Acknowledgments

This work was supported by the National Natural Science Foundation of China (grant Nos 41531174, 91425303, 91647104, and 41701426). We thank all the scientists, engineers, and students who participated in HiWATER field campaigns, and sincere appreciation is also extended to the Associate Editor (Dr. Tim R. McVicar), Editor, and four anonymous reviewers for their constructive comments on an earlier draft of this manuscript. The ground-measured data in this study were provided by the data center of the “Integrated research on the eco-hydrological process of the Heihe River Basin” (<http://www.heihedata.org/>) and the World Data System Cold and Arid Regions Science Data Center at Lanzhou (<http://card.westgis.ac.cn/>).

Appendix A

A.1. Measurements processing

Before using turbulent fluxes obtained from the EC system, all data were subjected to a quality assessment and control procedures (Liu et al., 2011). Table A1 shows the measurement heights, and the model number and manufacturer of each EC system. Latent and sensible heat fluxes were measured using 18 EC systems at a frequency of 10 Hz; data from 4 of the 22 ECs (the upper layer of Daman Superstation [#15], the Bajitan Gobi station [#18], the Shenshawo sandy desert station [#19], and the Huazhaizi desert steppe station [#20]) were not used to validate estimations of daily ET. To obtain high-quality flux data, EdiRE (<http://www.geos.ed.ac.uk/homes/jbm/micromet/EdiRe/>) and EddyPro (<https://www.licor.com/>

env/products/eddy_covariance/eddypro.html) software packages were used to process the EC data. The data processing procedures included spike detection, lag correction for H₂O/CO₂ relative to the vertical wind component, 2-D coordinate rotation, sonic virtual temperature correction, frequency response correction, and density fluctuation correction. The angle of attack (AOA) error correction was applied to the EC systems using a Gill-WindMaster sonic anemometer ([Liu et al., 2011, 2013](#)), and these measurements were converted to a 30-min average flux. Energy balance closure was not achieved at most stations, in which case the Bowen-ratio closure method ([Twine et al., 2000](#)) was used to force the energy balance.

At each of the 21 sites, net radiation was measured using CNR1 and CNR4 radiometers from Kipp & Zonen (Netherlands). Soil heat flux was measured using plates buried at a depth of 0.06 m, with 3 replicates at each site. Two plates were buried under bare soil, and the third was buried under plants. Surface soil heat flux (G_0) was calculated using the “PlateCal” approach ([Liebethal et al., 2005](#)), which is based on the weighted vegetation fraction, soil temperature, and moisture above the heat plates.

Table A1
EC systems and sensor heights of different sites during the HiWATER-MUSOEXE.

| Observation items | Model number, manufacturer | Site (height [m]) |
|--|--|---|
| Sensible and latent heat flux (eddy covariance system) | CSAT3/Li7500A, Campbell/Li-cor, USA | #4(4.2, 6.2 after Aug.19), #6(4.6), #7(3.8), #13(5), #15(lower layer 4.5, upper layer 34) |
| | CSAT3/Li7500, Campbell/Li-cor, USA | #2(3.7), #5(3), #8(3.2), #10(4.8), #11(3.5), #12(3.5), #14(4.6) |
| | CSAT3/EC150, Campbell, USA | #17(7) |
| | Gill/Li7500, Gill, UK and Li-cor, USA | #16(4.9) |
| | Gill/Li7500A, Gill, UK and Li-cor, USA | #1(3.8), #3(3.8), #9(3.9), #21(5.2) |

A.2. Satellite data pre-processing

MODIS LST, Quality Control (QC), and view time maps were acquired from the Terra 1-km data (MOD11A1, Collection 5). The albedo data, which have high spatiotemporal resolutions, were retrieved by fusing the daily MODIS surface reflectance data (250 to 500 m resolution) and the 16-day ETM+ surface reflectance data (30 m resolution). These daily albedo maps were resampled to 100 m using the area-weighted average method. LSTs were derived from the TIR band 61(60 m resolution) of ETM+ using radiative transfer theory (RTT) ([Yu et al., 2014](#)), and then resampled to 100 m. The normalized difference vegetation index (NDVI) was calculated from reflectance in the near-infrared and red bands, and fused using MODIS (1000 m resolution) and ETM+ (100 m resolution). The fractional vegetation cover (FVC) was then calculated from the NDVI:

$$FVC = 1 - \left(\frac{NDVI - NDVI_{max}}{NDVI_{min} - NDVI_{max}} \right)^K \quad (A1)$$

where $NDVI_{min}$ represents the NDVI of bare soil, $NDVI_{max}$ represents the maximum NDVI, and the constant K is 0.4631 ([Zhao and Ji, 2010](#)). The leaf area index (LAI) and emissivity were derived from the parametric relationships between the corresponding observations from HiWATER-MUSOEXE and the FVC. Canopy heights and building heights (HCHBs) were necessary for simulations of sensible heat. A remote sensing-based method was developed to construct daily dynamic maps of HCHBs for the growth season (April to October). In particular, high canopies (e.g., orchards) and high buildings (e.g., villages, residential buildings) were produced by [Xiao and Wen \(2013\)](#) using airborne LiDAR-DSM data. Short canopies (e.g., maize, barley, and vegetables) usually have seasonal variations, and the height of the short canopy (HCS) was calculated from NDVI as described by [Chen et al. \(2013a\)](#):

$$HCS = HCS_{min} + \frac{(NDVI - NDVI_{min})}{NDVI_{max} - NDVI_{min}} (HCS_{max} - HCS_{min}) \quad (A2)$$

where HCS_{max} and HCS_{min} are the maximum and minimum short canopy heights, respectively. HCS_{min} is set to 0.0012; and HCS_{max} is set to 2.05 m (the greatest height of seasonal crops during the growth season [April to October]). The last step was merging of data for high canopy heights and variable short canopy heights, and mapping of the HCHBs, which were used to calculate heat fluxes. Gaps in the ETM+ images were filled using the Geostatistical Neighborhood Similar Pixel Interpolator (GNSPI) ([Zhu et al., 2012](#)). The preprocessing of remote sensing data included geometric correction, subsetting, radiation calibration, and atmospheric correction for multisource remote sensing data.

Appendix B

B.1. SEBS model

The SEBS model determines the sensible heat flux by solving the similarity relationships for the profile of wind speed (u ; m/s) and the difference between potential temperature (θ_0 ; K) at the surface and the potential air temperature (θ_a ; K) at a reference height (z ; m) as:

$$H = ku_*\rho C_p(\theta_0 - \theta_a) \left[\ln\left(\frac{z - d_0}{z_{0h}}\right) - \psi_h\left(\frac{z - d_0}{L}\right) + \psi_h\left(\frac{z_{0h}}{L}\right) \right]^{-1} \quad (A3)$$

$$u = \frac{u_*}{k} \left[\ln\left(\frac{z - d_0}{z_{0m}}\right) - \Psi_m\left(\frac{z - d_0}{L}\right) + \Psi_h\left(\frac{z_{0m}}{L}\right) \right] \quad (\text{A4})$$

$$L = -\frac{\rho C_p u_*^3 \theta_v}{kgH} \quad (\text{A5})$$

where k is the von Kármán constant (0.4), u_* is the friction velocity (m/s), ρ is the density of air (kg/m^3), C_p is the specific heat of air at constant pressure ($\text{J kg}^{-1} \text{K}^{-1}$), z is the measurement height above the surface (m), u is the wind speed at reference height z (m/s), d_0 is the zero-plane displacement height (m), g is the acceleration due to gravity (9.8 m/s^2), θ_v is the potential virtual temperature near the surface (K), z_{0m} and z_{0h} are the roughness heights for momentum and heat transfer (m), H is the sensible heat flux (W/m^2), and Ψ_m and Ψ_h are the stability correction functions for momentum and sensible heat transfer for stable atmosphere conditions (Brutsaert, 1999) and unstable atmosphere conditions (Beljaars and Holtslag, 1991; van den Hurk and Holtslag, 1997), and L is the Monin-Obukhov length (m).

B.2. Fetch (Ω) of the z_{0m}

Over heterogeneous surfaces, such as our study area, z_{0m} can be direction-dependent (Zhang et al., 2004; Lu et al., 2009). Fig. A1 demonstrates that z_{0m} at P_0 is impacted by the windward direction of many roughness elements in the fetch (i.e., the fanlike area [Ω]), which was mapped using an arc and two straight border lines that form 30° fanlike arcs along the windward side. For example, for the z_{0m} at $P_0(x_0, y_0)$, the HCHB(x, y) represents roughness elements (canopy height and building height) at $P(x, y)$ in the fanlike area, and $D(x, y)$ represents the distance between a point $P(x, y)$ and the measured point $P_0(x_0, y_0)$. Because our experimental area is heterogeneous, there are many different roughness elements, and the corresponding equivalent geometric roughness values (η) were therefore different. The equivalent geometric roughness could have a considerable effect on the z_{0m} . A model as described in Eqs. (2) and (3) was employed to convert the equivalent geometric roughness within the fetch to the surface roughness length for determination of momentum transfer (z_{0m}).

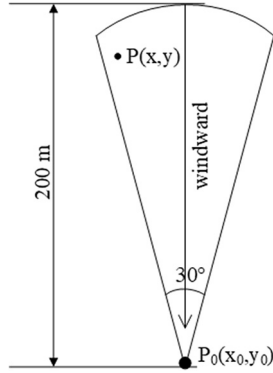


Fig. A1. Fetch area (Ω) of z_{0m} at P_0 .

B.3. ESTARFM

ESTARFM described by Zhu et al. (2010) is a linear model (Eq. (A6)). In this algorithm, the predicted fine-resolution Landsat-like VNIR/SWIR reflectance bands and TIR bands at radiance level are directly calculated using two pairs of fine- and coarse-resolution images at t_a and t_c (in which t_a and t_c are the acquisition dates for one pair of fine- and coarse-resolution images), and the coarse resolution image at the prediction time (t_p) is only used to calculate the temporal weight at t_a and t_c .

$$F_p(x_{w/2}, y_{w/2}, t_p, O) = [T_a^p F(x_{w/2}, y_{w/2}, t_a, O) + T_c^p F(x_{w/2}, y_{w/2}, t_c, O)] + \sum_{i=1}^N W_i V_i \begin{bmatrix} T_a^p (C(x_i, y_i, t_p, O) - C(x_i, y_i, t_a, O)) \\ + T_c^p (C(x_i, y_i, t_p, O) - C(x_i, y_i, t_c, O)) \end{bmatrix}, \quad (O = r/O = T_{radiance}) \quad (\text{A6})$$

$$T_k^p = \frac{1 / \left| \sum_{i=1}^w \sum_{j=1}^w C(x_i, y_i, t_k, O) - \sum_{i=1}^w \sum_{j=1}^w C(x_i, y_i, t_p, O) \right|}{\sum_{k=a,c} \left(1 / \left| \sum_{i=1}^w \sum_{j=1}^w C(x_i, y_i, t_k, O) - \sum_{i=1}^w \sum_{j=1}^w C(x_i, y_i, t_p, O) \right| \right)} \quad (\text{A7})$$

where F_p is the final predicted fine-resolution image at t_p , F and C denote the fine- and coarse- resolution images, O is the single-band VNIR/SWIR reflectance band (r) or TIR band at radiance level ($T_{radiance}$), N is the number of similar pixels including the central “prediction” pixel within the search window, (x_i, y_i) is the location of the i th similar pixel, W_i is the weight of the i th similar pixel, V_i is the conversion coefficient of the i th similar pixel, T_a^p and T_c^p are the temporal weights at t_a and t_c (calculated from the change in magnitude from the resampled coarse-resolution images between the time [t_a or t_c] and the prediction time t_p), and w is the size of the window (set to 20×20 for single-band reflectance images and 15×15 for radiance images).

Appendix C

C.1. Analysis of residual error

We determined residual errors (estimated ET – observed ET) to quantify the impacts of observed ET, net radiation (R_n), meteorological variables (atmospheric vapor pressure deficit [VPD], dT , and wind speed), soil moisture (volumetric water content [VWC]), and surface vegetation (LAI) on error propagation in the estimation of HiTLL ET (Fig. A2). In Fig. A2a, the residual error had a negative correlation ($R = -0.38$) with the observed ET. Fig. A2a also demonstrates that ET were slightly overestimated when the ET observations and VWC were low (i.e., ET observations < 3 mm/day, VWC < 15%), but these estimates improved as ET and VWC increased. The residual error had a weak negative correlation ($R = -0.01$) with measured R_n (Fig. A2b) at high R_n values ($> 450 \text{ W/m}^2$). However, the residual error had a positive correlation with LST ($R = 0.42$) for LST values of 300 to 325 K and VWC values of 5% to 15% (Fig. A2c). Fig. 4h shows that the residual ET errors had a weak correlation with dT when it was below 5 K. The residual error was evenly distributed across the entire ranges of VPD, wind speed, LAI, and VWC (Fig. A2d, e, f, and g).

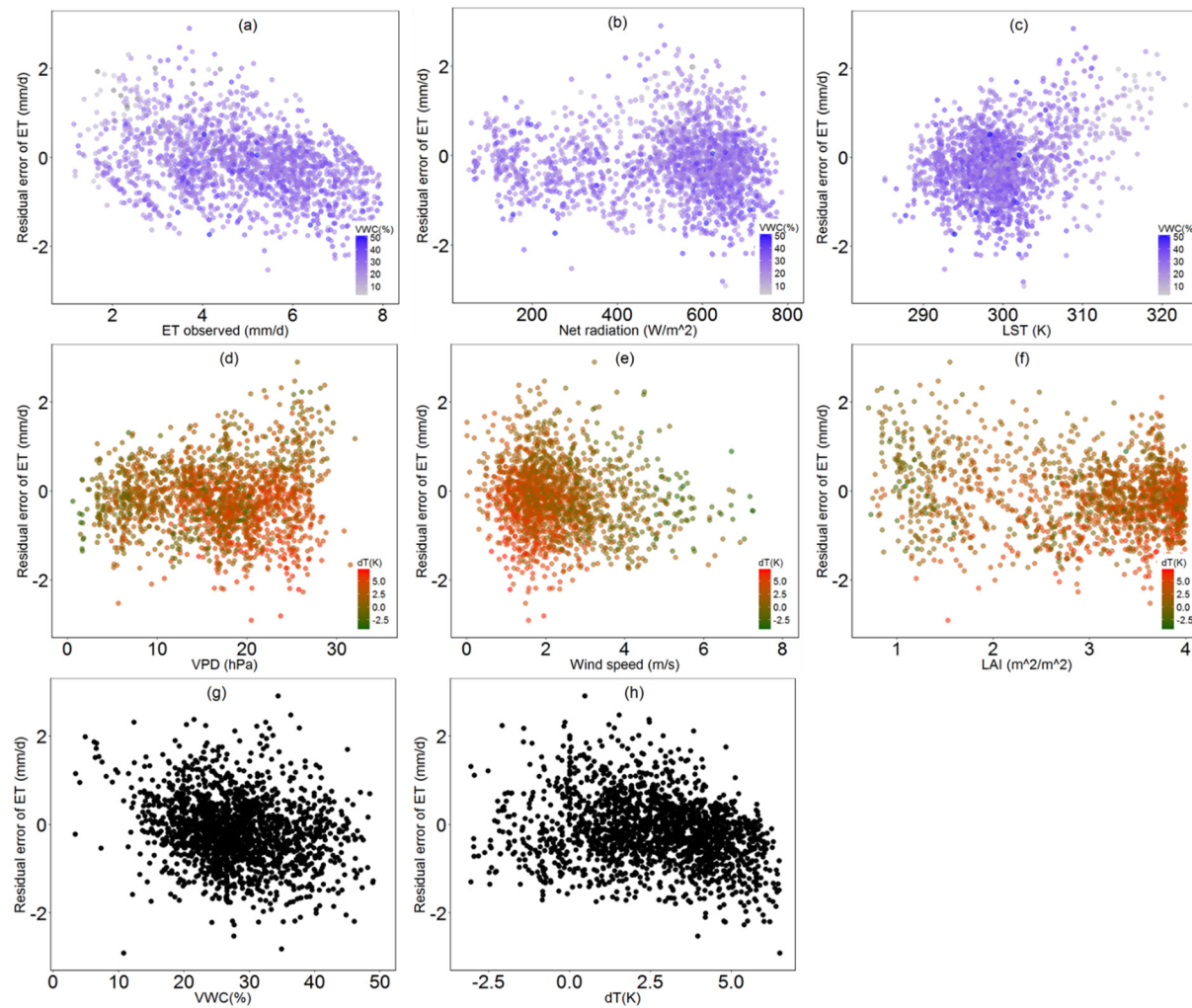


Fig. A2. Relationship of residual error in ET estimates (ordinate) with environmental and land surface variables (abscissa) derived from the HiTLL scheme.

C.2. Histograms for the differences between monthly remotely sensed ET products and HiTLL ET

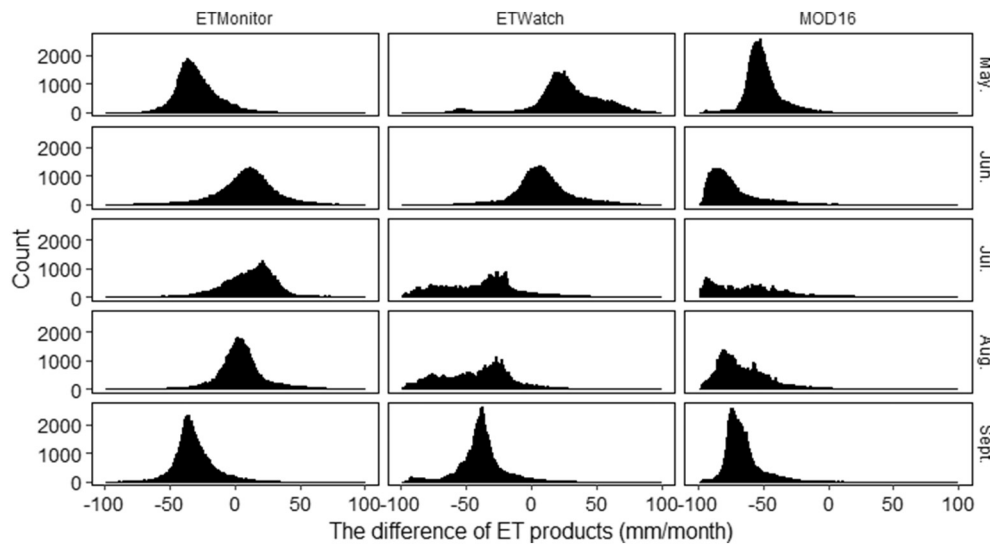


Fig. A3. Histograms for the differences of three monthly ET remote sensing products and HiTLL ET (this study) in the midstream of the oasis of the HRB (May to September 2012). Column1: ETMonitor – HiTLL ET; Column 2: ETWatch – HiTLL ET; Column 3: MOD16 – HiTLL ET.

C.3. Mapping coarser resolution ET

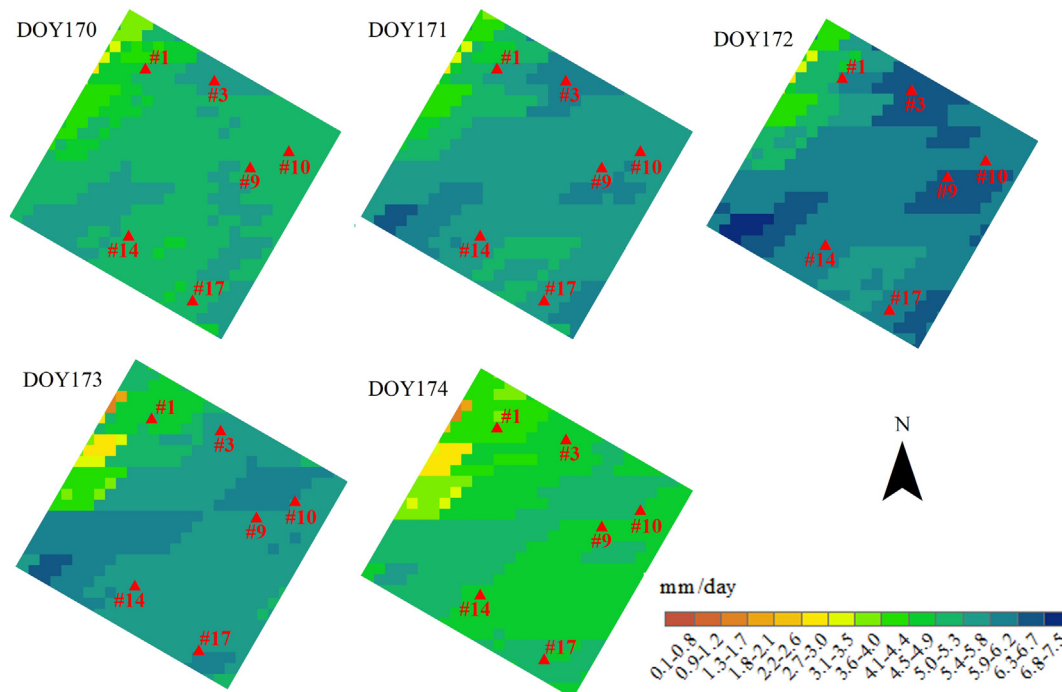


Fig. A4. Daily ET product derived from the Daily ET Datasets (2012) (1000 m resolution; Zhou et al., 2014) in the KEA (5.5 km × 5.5 km) during an irrigation period (DOY170 to DOY174, 2012).

References

- Agam, N., Kustas, W.P., Anderson, M.C., Li, F., Neale, C.M.U., 2007. A vegetation index based technique for spatial sharpening of thermal imagery. *Remote Sens. Environ.* 107 (4), 545–558. <https://doi.org/10.1016/j.rse.2006.10.006>.
- Agam, N., Kustas, W.P., Anderson, M.C., Li, F., Colaizzi, P.D., 2008. Utility of thermal image sharpening for monitoring field-scale evapotranspiration over rainfed and irrigated agricultural regions. *Geophys. Res. Lett.* 35 (2), 196–199. <https://doi.org/10.1029/2007GL032195>.
- Ahadi, R., Samani, Z., Skaggs, R., 2013. Evaluating on-farm irrigation efficiency across the watershed: a case study of New Mexico's Lower Rio Grande Basin. *Agric. Water Manag.* 124 (124), 52–57. <https://doi.org/10.1016/j.agwat.2013.03.010>.
- Alfieri, J.G., Anderson, M.C., Kustas, W.P., Cammalleri, C., 2017. Effect of the revisit interval and temporal upscaling methods on the accuracy of remotely sensed evapotranspiration estimates. *Hydrol. Earth Syst. Sci.* 21, 83–98. <https://doi.org/10.5194/hess-21-83-2017>.
- Allen, R.G., Tasumi, M., Morse, A., Trezza, R., 2005. A Landsat-based energy balance and evapotranspiration model in Western US water rights regulation and planning. *Irrig. Drain. Syst.* 19 (3–4), 251–268. <https://doi.org/10.1007/s10795-005-5187-z>.
- Allen, R.G., Rohison, C.W., Ricardo, T., Magali, G., Jeppe, K., 2008. Comparison of evapotranspiration images from MODIS and Landsat along the Middle Rio Grande of

- New Mexico. In: The 17th William T. Pecora Memorial Remote Sensing Symposium Proceedings, Denver, Colorado, . <http://www.asprs.org/a/publications/proceedings/pecora17/0003.pdf>.
- Anderson, M.C., Norman, J.M., Mecikalski, J.R., Otkin, J.A., Kustas, W.P., 2007. A climatological study of evapotranspiration and moisture stress across the continental United States based on thermal remote sensing: 2. Surface moisture climatology. *J. Geophys. Res. Atmos.* 112 (D10), 1–13. <https://doi.org/10.1029/2006JD007506>.
- Anderson, M.C., Norman, J.M., Kustas, W.P., Houborg, R., Starks, P.J., Agam, N., 2008. A thermal-based remote sensing technique for routine mapping of land-surface carbon, water and energy fluxes from field to regional scales. *Remote Sens. Environ.* 112 (12), 4227–4241. <https://doi.org/10.1016/j.rse.2008.07.009>.
- Anderson, M.C., Kustas, W.P., Norman, J.M., Hain, C.R., 2011. Mapping daily evapotranspiration at field to continental scales using geostationary and polar orbiting satellite imagery. *Hydrol. Earth Syst. Sci.* 15 (1), 223–239. <https://doi.org/10.5194/hess-15-223-2011>.
- Anderson, M.C., Allen, R.G., Morse, A., Kustas, W.P., 2012a. Use of Landsat thermal imagery in monitoring evapotranspiration and managing water resources. *Remote Sens. Environ.* 122, 50–55. <https://doi.org/10.1016/j.rse.2011.08.025>.
- Anderson, M.C., Kustas, W.P., Alfieri, J.G., Gao, F., Hain, C., Prueger, J.H., Evett, S., Colaizzi, P., Howell, T., Chávez, J.L., 2012b. Mapping daily evapotranspiration at Landsat spatial scales during the BEAREX'08 field campaign. *Adv. Water Resour.* 50, 162–177. <https://doi.org/10.1016/j.advwatres.2012.06.005>.
- Bai, J., Jia, L., Liu, S., Xu, Z., Hu, G., Zhu, M., Song, L., 2015. Characterizing the footprint of eddy covariance system and large aperture scintillometer measurements to validate satellite-based surface fluxes. *IEEE Geosci. Remote Sens. Lett.* 12 (5), 943–947. <https://doi.org/10.1109/LGRS.2014.2368580>.
- Bai, L., Cai, J., Liu, Y., Chen, H., Zhang, B., Huang, L., 2017. Responses of field evapotranspiration to the changes of cropping pattern and groundwater depth in large irrigation district of Yellow River Basin. *Agric. Water Manag.* 188, 1–11. <https://doi.org/10.1016/j.agwat.2017.03.028>.
- Barsi, J.A., Schott, J.R., Palluconi, F.D., Hook, S.J., 2005. Validation of a web-based atmospheric correction tool for single thermal band instruments. In: Proc. SPIE. vol. 5822 SPIE, Bellingham, WA. <https://doi.org/10.1117/12.619990>.
- Bastiaanssen, W.G.M., Brito, R.A.L., Bos, M.G., Souza, R.A., Cavalanti, E.B., Bakker, M.M., 2001. Low cost satellite data for monthly irrigation performance monitoring: benchmarks from Nilo Coelho, Brazil. *Irrig. Drain. Syst.* 15 (1), 53–79. <https://doi.org/10.1023/A:101796702119>.
- Bastiaanssen, W.G.M., Noordman, E.J.M., Pelgrum, H., Davids, G., Thoreson, B.P., Allen, R.G., 2005. SEBAL model with remotely sensed data to improve water-resources management under actual field conditions. *J. Irrig. Drain. Eng.* 131 (1), 85–93. [https://doi.org/10.1061/\(ASCE\)0733-9437\(2005\)131:1\(85\)](https://doi.org/10.1061/(ASCE)0733-9437(2005)131:1(85)).
- Battude, M., Bitar, A.A., Brut, A., Tallec, T., Huc, M., Cros, J., Weber, J.J., Lhuissier, L., Simonneaux, V., Demarez, V., 2017. Modeling water needs and total irrigation depths of maize crop in the south west of France using high spatial and temporal resolution satellite imagery. *Agric. Water Manag.* 189, 123–136. <https://doi.org/10.1016/j.agwat.2017.04.018>.
- Beljaars, A.C.M., Holtslag, A.A.M., 1991. Flux parameterization over land surfaces for atmospheric models. *J. Appl. Meteorol.* 30 (3), 327–341. [https://doi.org/10.1175/1520-0450\(1991\)030<0327:FPOLSF>2.0.CO;2](https://doi.org/10.1175/1520-0450(1991)030<0327:FPOLSF>2.0.CO;2).
- Berbigier, P., Bonnefond, J.M., Mellmann, P., 2001. CO₂ and water vapour fluxes for 2 years aboveveeuroflux forest site. *Agric. For. Meteorol.* 108 (3), 183–197. [https://doi.org/10.1016/S0168-1923\(01\)00240-4](https://doi.org/10.1016/S0168-1923(01)00240-4).
- Bernstein, L.S., Jin, X., Gregor, B., Adler-Golden, S., 2012. Quick atmospheric correction code: algorithm description and recent upgrades. *Opt. Eng.* 51 (11), 111719–1–111719–11. <https://doi.org/10.1117/1.OE.51.11.111719>.
- Bindhu, V.M., Narasimhan, B., Sudheer, K.P., 2013. Development and verification of a non-linear disaggregation method (NL-DisTrad) to downscale MODIS land surface temperature to the spatial scale of Landsat thermal data to estimate evapotranspiration. *Remote Sens. Environ.* 135, 118–129. <https://doi.org/10.1016/j.rse.2013.03.023>.
- Bosveld, F.C., Holtslag, A.A.M., Van Den Hurk, B.J.J.M., 1999. Interpretation of crown radiation temperatures of a dense Douglas fir forest with similarity theory. *Bound.-Layer Meteorol.* 92 (3), 429–451. <https://doi.org/10.1023/A:1002087526720>.
- Brutsaert, W., 1999. Aspects of bulk atmospheric boundary layer similarity under free-convective conditions. *Rev. Geophys.* 37 (4), 439–451. <https://doi.org/10.1029/1999RG900013>.
- Cammalleri, C., Ciraolo, G., Minacapilli, M., 2008. Spatial sharpening of land surface temperature for daily energy balance applications. *Remote Sens. Agric. Ecosyst. Hydrol. X* 7104, 71040J. <https://doi.org/10.1117/12.800328>.
- Cammalleri, C., Anderson, M.C., Gao, F., Hain, C.R., Kustas, W.P., 2013. A data fusion approach for mapping daily evapotranspiration at field scale. *Water Resour. Res.* 49 (8), 4672–4686. <https://doi.org/10.1002/wrcr.20349>.
- Cammalleri, C., Anderson, M.C., Kustas, W.P., 2014a. Upscaling of evapotranspiration fluxes from instantaneous to daytime scales for thermal remote sensing applications. *Hydrol. Earth Syst. Sci.* 18 (5), 1885–1894. <https://doi.org/10.5194/hess-18-1885-2014>.
- Cammalleri, C., Anderson, M.C., Gao, F., Hain, C.R., Kustas, W.P., 2014b. Mapping daily evapotranspiration at field scales over rainfed and irrigated agricultural areas using remote sensing data fusion. *Agric. For. Meteorol.* 186, 1–11. <https://doi.org/10.1016/j.agrformet.2013.11.001>.
- Chen, D.J., Xu, Z.M., Chen, R.S., 2003. Design of water resources accounts: a case of integrated environmental and economic accounting. *Adv. Water Sci.* 14 (5), 637–641. <https://doi.org/10.14042/j.cnki.32.1309.2003.05.019>.
- Chen, X., Su, Z., Ma, Y., Yang, K., Wen, J., Zhang, Y., 2013a. An improvement of roughness height parameterization of the Surface Energy Balance System (SEBS) over the Tibetan Plateau. *J. Appl. Meteorol. Climatol.* 52 (3), 607–622. <https://doi.org/10.1175/JAMC-D-12-056.1>.
- Chen, X., Su, Z., Ma, Y., Yang, K., Wang, B., 2013b. Estimation of surface energy fluxes under complex terrain of Mt. Qomolangma over the Tibetan Plateau. *Hydrol. Earth Syst. Sci.* 17, 1607–1618. <https://doi.org/10.5194/hess-17-1607-2013>.
- Chen, X., Su, Z., Ma, Y., Liu, S., Yu, Q., Xu, Z., 2014. Development of a 10-year (2001–2010) 0.1° data set of land-surface energy balance for mainland China. *Atmos. Chem. Phys.* 14 (23), 14471–14518. <http://hdl.handle.net/10453/36164>.
- Cheng, G., Li, X., Zhao, W., Xu, Z., Feng, Q., Xiao, S., Xiao, H., 2014. Integrated study of the water–ecosystem–economy in the Heihe River Basin. *Nat. Sci. Rev.* 1 (3), 413–428. <https://doi.org/10.1093/nsr/nwu017>.
- Cheng, Y., Sayde, C., Li, Q., Basara, J., Selker, J., Tanner, E., Gentine, P., 2017. Failure of Taylor's hypothesis in the atmospheric surface layer and its correction for eddy-covariance measurements. *Geophys. Res. Lett.* 44 (9), 4287–4295. <https://doi.org/10.1002/2017GL073499>.
- Chirouze, J., Boulet, G., Jarlan, L., Fieuval, R., Rodriguez, J.C., Ezzahar, J., Er-Raki, S., Bigeard, G., Merlin, O., Garatuza-Payan, J., Watts, C., Chehbouni, G., 2014. Intercomparison of four remote-sensing-based energy balance methods to retrieve surface evapotranspiration and water stress of irrigated fields in semi-arid climate. *Hydrol. Earth Syst. Sci.* 18 (3), 1165–1188. <https://doi.org/10.5194/hess-18-1165-2014>.
- Choi, M., Kustas, W.P., Anderson, M.C., Allen, R.G., Li, F., Kjaersgaard, J.H., 2009. An intercomparison of three remote-sensing-based surface energy balance algorithms over a corn and soybean production region (Iowa, U.S.) during SMACEX. *Agric. For. Meteorol.* 149 (12), 2082–2097. <https://doi.org/10.1016/j.agrformet.2009.07.002>.
- Droogers, P., Immerzeel, W.W., Lorite, I.J., 2010. Estimating actual irrigation application by remotely sensed evapotranspiration observations. *Agric. Water Manag.* 97 (9), 1351–1359. <https://doi.org/10.1016/j.agwat.2010.03.017>.
- Duan, S.B., Li, Z.L., Leng, P., 2017. A framework for the retrieval of all-weather land surface temperature at a high spatial resolution from polar-orbiting thermal infrared and passive microwave data. *Remote Sens. Environ.* 195, 107–117. <https://doi.org/10.1016/j.rse.2017.04.008>.
- Elnesr, M., Alazba, A., 2013. Effect of climate change on spatiotemporal variability and trends of evapotranspiration, and its impact on water resources management in the Kingdom of Saudi Arabia. In: Climate Change-Realities, Impacts Over Ice Cap, Sea Level and Risks. InTech. <https://doi.org/10.5772/54832>.
- Emelyanova, I.V., McVicar, T.R., Van Niel, T.G., Li, L.T., van Dijk, A.I., 2013. Assessing the accuracy of blending Landsat–MODIS surface reflectances in two landscapes with contrasting spatial and temporal dynamics: a framework for algorithm selection. *Remote Sens. Environ.* 133, 193–209. <https://doi.org/10.1016/j.rse.2013.02.007>.
- Eswar, R., Sekhar, M., Bhattacharya, B.K., 2013. A simple model for spatial disaggregation of evaporative fraction: comparative study with thermal sharpened land surface temperature data over India. *J. Geophys. Res. Atmos.* 118 (21), 12,029–12,044. <https://doi.org/10.1020/2013JD020813>.
- Eswar, R., Sekhar, M., Bhattacharya, B.K., Bandyopadhyay, S., 2017. Spatial disaggregation of latent heat flux using contextual models over India. *Remote Sens.* 9 (9), 949. <https://doi.org/10.3390/rs9090949>.
- Fereres, E., Soriano, M.A., 2007. Deficit irrigation for reducing agricultural water use. *J. Exp. Bot.* 58 (2), 147–159. <https://doi.org/10.1093/jxb/erl165>.
- Fraiture, C.D., Wichelns, D., 2010. Satisfying future water demands for agriculture. *Agric. Water Manag.* 97 (4), 502–511. <https://doi.org/10.1016/j.agwat.2009.08.008>.
- Gao, Y., Long, D., 2008. Intercomparison of remote sensing-based models for estimation of evapotranspiration and accuracy assessment based on SWAT. *Hydrol. Process.* 22 (25), 4850–4869. <https://doi.org/10.1002/hyp.7104>.
- Gao, F., Masek, J., Schwaller, M., Hall, F., 2006. On the blending of the Landsat and MODIS surface reflectance: predicting daily Landsat surface reflectance. *IEEE Trans. Geosci. Remote Sens.* 44 (8), 2207–2218. <https://doi.org/10.1109/TGRS.2006.872081>.
- Gao, F., Anderson, M.C., Zhang, X., Yang, Z., Alfieri, J.G., Kustas, W.P., Mueller, R., Johnson, D.M., Prueger, J.H., 2017. Toward mapping crop progress at field scales through fusion of Landsat and MODIS imagery. *Remote Sens. Environ.* 188, 9–25. <https://doi.org/10.1016/j.rse.2016.11.004>.
- Ge, Y., Zhuang, J., Xu, F., Huang, Y., Ma, C., Wang, W., 2013. HiWATER: Dataset of Measurements on Channel Flow in the Middle Reaches of the Heihe River Basin. *Heihe Plan Science Data Center* <https://doi.org/10.3972/hiwater.123.2013.db>.
- Gevaert, C.M., García-Haro, F.J., 2015. A comparison of STARFM and an unmixing-based algorithm for Landsat and MODIS data fusion. *Remote Sens. Environ.* 156, 34–44. <https://doi.org/10.1016/j.rse.2014.09.012>.
- Gokmen, M., Vekerdy, Z., Verhoef, A., Verelaan, O., van der Tol, C., 2012. Integration of soil moisture in SEBS for improving evapotranspiration estimation under water stress conditions. *Remote Sens. Environ.* 121, 261–274. <https://doi.org/10.1016/j.rse.2012.02.003>.
- Gu, L., Meyers, T., Pallardy, S.G., Hanson, P.J., Yang, B., Heuer, M., Hosman, K.P., Riggs, J.S., Sluss, D., Wullschleger, S.D., 2006. Direct and indirect effects of atmospheric conditions and soil moisture on surface energy partitioning revealed by a prolonged drought at a temperate forest site. *J. Geophys. Res. Atmos.* 111 (D16). <https://doi.org/10.1029/2006JD007161>.
- Hong, S.H., Hendrickx, J.M.H., Borchers, B., 2011. Down-scaling of SEBAL derived evapotranspiration maps from MODIS (250 m) to Landsat (30 m) scales. *Int. J. Remote Sens.* 32 (21), 6457–6477. <https://doi.org/10.1080/01431161.2010.512929>.
- Hu, Z.L., Islam, S., 1997. A framework for analyzing and designing scale invariant remote sensing algorithms. *IEEE Trans. Geosci. Remote Sens.* 35 (3), 747–755. <https://doi.org/10.1109/36.581996>.
- Jackson, R.D., Hatfield, J.L., Regnato, R.J., Idso, S.B., Pinter Jr., P.J., 1983. Estimation of daily evapotranspiration from one time-of-day measurements. *Agric. Water Manag.* 7 (1–3), 351–362. [https://doi.org/10.1016/0378-3774\(83\)90095-1](https://doi.org/10.1016/0378-3774(83)90095-1).
- Jarihani, A., McVicar, T.R., van Niel, T., Emelyanova, I., Callow, J., Johansen, K., 2014.

- Blending landsat and modis data to generate multispectral indices: a comparison of “index-then-blend” and “blend-then-index” approaches. *Remote Sens.* 6 (10), 9213–9238. <https://doi.org/10.3390/rs6109213>.
- Jia, L., Su, Z., van den Hurk, B., Menenti, M., Moene, A., De Bruin, H.A., Yrisarry, J.J.B., Ibanez, M., Cuesta, A., 2003. Estimation of sensible heat flux using the Surface Energy Balance System (SEBS) and ATSR measurements. *Phys. Chem. Earth A/B/C* 28 (1–3), 75–88. [https://doi.org/10.1016/S1474-7065\(03\)00009-3](https://doi.org/10.1016/S1474-7065(03)00009-3).
- Jia, Z., Liu, S., Xu, Z., Chen, Y., Zhu, M., 2012. Validation of remotely sensed evapotranspiration over the Hai River Basin, China. *J. Geophys. Res. Atmos.* 117 (D13). <https://doi.org/10.1029/2011JD017037>.
- Jia, L., Hu, G., Cui, Y., 2014. The Evapotranspiration Data From May to September of 2012 in the Heihe River Basin. Heihe Plan Science Data Center <https://doi.org/10.3972/heihe.006.2014.db>.
- Kalma, J.D., McVicar, T.R., McCabe, M.F., 2008. Estimating land surface evaporation: a review of methods using remotely sensed surface temperature data. *Surv. Geophys.* 29 (4–5), 421–469. <https://doi.org/10.1007/s10712-008-9037-z>.
- Kanda, M., Kanega, M., Kawai, T., Moriaki, R., Sugawara, H., 2007. Roughness lengths for momentum and heat derived from outdoor urban scale models. *J. Appl. Meteorol. Climatol.* 46 (7), 1067–1079. <https://doi.org/10.1175/JAM2500.1>.
- Kang, J., Jin, R., Li, X., 2015. Regression kriging-based upscaling of soil moisture measurements from a wireless sensor network and multiresource remote sensing information over heterogeneous cropland. *IEEE Geosci. Remote Sens. Lett.* 12 (1), 92–96. <https://doi.org/10.1109/LGRS.2014.2326775>.
- Kormann, R., Meixner, F.X., 2001. An analytical footprint model for non-neutral stratification. *Bound.-Layer Meteorol.* 99 (2), 207–224. <https://doi.org/10.1023/A:1018991015119>.
- Kustas, W.P., Daughtry, C.S.T., 1990. Estimation of the soil heat flux/net radiation ratio from spectral data. *Agric. For. Meteorol.* 49 (3), 205–223. [https://doi.org/10.1016/0168-1923\(90\)90033-3](https://doi.org/10.1016/0168-1923(90)90033-3).
- Kustas, W.P., Norman, J.M., Anderson, M.C., French, A.N., 2003. Estimating subpixel surface temperatures and energy fluxes from the vegetation index – radiometric temperature relationship. *Remote Sens. Environ.* 85 (4), 429–440. [https://doi.org/10.1016/S0034-4257\(03\)00036-1](https://doi.org/10.1016/S0034-4257(03)00036-1).
- Kustas, W.P., Nieto, H., Morillas, L., Anderson, M.C., Alfieri, J.G., Hipps, L.E., Villagarcía, L., Domingo, F., García, M., 2016. Revisiting the paper “Using radiometric surface temperature for surface energy flux estimation in Mediterranean drylands from a two-source perspective”. *Remote Sens. Environ.* 184, 645–653. <https://doi.org/10.1016/j.rse.2016.07.024>.
- Li, X., Cheng, G., Liu, S., Xiao, Q., Ma, M., Jin, R., Che, T., Liu, Q., Wang, W., Qi, Y., Wen, J., Li, H., Zhu, G., Guo, J., Ran, Y., Wang, S., Zhu, Z., Zhou, J., Hu, X., Xu, Z., 2013. Heihe watershed allied telemetry experimental research (HiWATER): scientific objectives and experimental design. *Bull. Am. Meteorol. Soc.* 94 (8), 1145–1160. <https://doi.org/10.1175/BAMS-D-12-00154.1>.
- Li, Y., Huang, C., Hou, J., Gu, J., Zhu, G., Li, X., 2017. Mapping daily evapotranspiration based on spatiotemporal fusion of ASTER and MODIS images over irrigated agricultural areas in the Heihe River Basin, Northwest China. *Agric. For. Meteorol.* 244–245, 82–97. <https://doi.org/10.1016/j.agrformet.2017.05.023>.
- Li, X., Liu, S., Xiao, Q., Ma, M., Jin, R., Che, T., Wang, W., Hu, X., Xu, Z., Wen, J., Wang, L., 2017. A multiscale dataset for understanding complex eco-hydrological processes in a heterogeneous oasis system. *Sci. Data* 4, 170083. <https://doi.org/10.1038/sdata.2017.83>.
- Li, X.J., Xin, X., Jiao, J., Peng, Z., Zhang, H., Shao, S., Liu, Q., 2017. Estimating subpixel surface heat fluxes through applying temperature-sharpening methods to MODIS data. *Remote Sens.* 9 (8), 836. <https://doi.org/10.3390/rs9080836>.
- Li, X., Cheng, G., Ge, Y., Li, H., Han, F., Hu, X., Tian, W., Tian, Y., Pan, X., Nian, Y., Zhang, Y., Ran, Y., Zheng, Y., Gao, B., Yang, D., Zheng, C., Wang, X., Liu, S., Cai, X., 2018. Hydrological cycle in the Heihe River Basin and its implication for water resource management in endorheic basins. *J. Geophys. Res. Atmos.* 123 (2), 890–914. <https://doi.org/10.1002/2017JD027889>.
- Liebethal, C., Huwe, B., Foken, T., 2005. Sensitivity analysis for two ground heat flux calculation approaches. *Agric. For. Meteorol.* 132 (3–4), 253–262. <https://doi.org/10.1016/j.agrformet.2005.08.001>.
- Liou, Y.A., Kar, S.K., 2014. Evapotranspiration estimation with remote sensing and various surface energy balance algorithms—a review. *Energies* 7 (5), 2821–2849. <https://doi.org/10.3390/en7052821>.
- Liou, Y.A., Kim, E.J., England, A.W., 1998. Radiobrightness of prairie soil and grassland during dry-down simulations. *Radio Sci.* 33 (2), 259–265. <https://doi.org/10.1029/97RS03655>.
- Liu, X., Bo, Y., 2015. Object-based crop species classification based on the combination of airborne hyperspectral images and lidar data. *Remote Sens.* 7 (1), 922–950. <https://doi.org/10.3390/rs70100922>.
- Liu, S., Hu, G., Lu, L., Mao, D., 2007a. Estimation of regional evapotranspiration by TM/ETM + data over heterogeneous surfaces. *Photogramm. Eng. Remote. Sens.* 73 (10), 1169–1178. <https://doi.org/10.14358/PERS.73.10.1169>.
- Liu, S., Lu, L., Mao, D., Jia, L., 2007b. Evaluating parameterizations of aerodynamic resistance to heat transfer using field measurements. *Hydrol. Earth Syst. Sci.* 11 (2), 769–783. <https://doi.org/10.5194/hess-11-769-2007>.
- Liu, S., Xu, Z., Wang, W., Jia, Z., Zhu, M., Bai, J., Wang, J., 2011. A comparison of eddy-covariance and large aperture scintillometer measurements with respect to the energy balance closure problem. *Hydrol. Earth Syst. Sci.* 15, 1291–1306. <https://doi.org/10.5194/hess-15-1291-2011>.
- Liu, S., Xu, Z., Zhu, Jia, Z., Zhu, M., 2013. Measurements of evapotranspiration from eddy-covariance systems and large aperture scintillometers in the Hai River Basin, China. *J. Hydrol.* 487, 24–38. <https://doi.org/10.1016/j.jhydrol.2013.02.025>.
- Liu, Y., Zhuang, Q., Chen, M., Pan, Z., Tchekabakova, N., Sokolov, A., Kicklighter, D., Melillo, J., Sirin, A., Zhou, G., He, Y., Chen, J., Bowling, L., Miralles, D., Parfenova, E., 2013. Response of evapotranspiration and water availability to changing climate and land cover on the Mongolian Plateau during the 21st century. *Glob. Planet. Chang.* 108, 85–99. <https://doi.org/10.1016/j.gloplacha.2013.06.008>.
- Liu, Y., Zhuang, Q., Pan, Z., Miralles, D., Tchekabakova, N., Kicklighter, D., Chen, J., Sirin, A., He, Y., Zhou, G., Melillo, J., 2014. Response of evapotranspiration and water availability to the changing climate in Northern Eurasia. *Clim. Chang.* 126 (3–4), 413–427. <https://doi.org/10.1007/s10584-014-1234-9>.
- Liu, Y., Pan, Z., Zhuang, Q., Miralles, D.G., Teuling, A.J., Zhang, T., An, P., Dong, Z., Zhang, J., He, D., Wang, L., Pan, X., Bai, W., Niayogi, D., 2015. Agriculture intensifies soil moisture decline in Northern China. *Sci. Rep.* 5, 11261. <https://doi.org/10.1038/srep11261>.
- Liu, S., Xu, Z., Song, L., Zhao, Q., Ge, Y., Xu, T., Ma, Y., Zhu, Z., Jia, Z., Zhang, F., 2016. Upscaling evapotranspiration measurements from multi-site to the satellite pixel scale over heterogeneous land surfaces. *Agric. For. Meteorol.* 230–231, 97–113. <https://doi.org/10.1016/j.agrformet.2016.04.008>.
- Lu, L., Liu, S.M., Xu, Z.W., Yang, K., Cai, X.H., Jia, L., Wang, J.M., 2009. The characteristics and parameterization of aerodynamic roughness length over heterogeneous surfaces. *Adv. Atmos. Sci.* 26 (1), 180–190. <https://doi.org/10.1007/s00376-009-0180-3>.
- Ma, Y., Liu, S., Zhang, F., Zhou, J., Jia, Z., Song, L., 2015. Estimations of regional surface energy fluxes over heterogeneous oasis–desert surfaces in the middle reaches of the Heihe River during HiWATER-MUSOEXE. *IEEE Geosci. Remote Sens. Lett.* 12 (3), 671–675. <https://doi.org/10.1109/LGRS.2014.2356652>.
- Mallick, K., Jarvis, A.J., Boegh, E., Fisher, J.B., Drewry, D.T., Tu, K.P., Hook, S.J., Hulley, G., Ardöö, J., Beringer, J., Arain, A., Niayogi, D., 2014. A Surface Temperature Initiated Closure (STIC) for surface energy balance fluxes. *Remote Sens. Environ.* 141, 243–261. <https://doi.org/10.1016/j.rse.2013.10.022>.
- Mallick, K., Boegh, E., Trebs, I., Alfieri, J.G., Kustas, W.P., Prueger, J.H., Niayogi, D., Das, N., Drewry, D.T., Hoffmann, L., Jarvis, A.J., 2015. Reintroducing radiometric surface temperature into the Penman–Monteith formulation. *Water Resour. Res.* 51 (8), 6214–6243. <https://doi.org/10.1002/2014WR016106>.
- Mallick, K., Trebs, I., Boegh, E., Giustarini, L., Schlerf, M., Drewry, D.T., Hoffmann, L., von Randow, C., Kruijt, B., Aratijo, A., Saleska, S., Ehleringer, J.R., Domingues, T.F., Ometto, J.P.H.B., Nobre, A.D., de Moraes, O.L.L., Hayek, M., Munger, J.W., Wofsy, S.C., 2016. Canopy-scale biophysical controls of transpiration and evaporation in the Amazon Basin. *Hydrol. Earth Syst. Sci.* 20 (10), 4237–4264. <https://doi.org/10.5194/hess-20-4237-2016>.
- Martin, T.C., Allen, R.G., Brazil, L.E., Burkhalter, J.P., Polly, J.S., 2013. Evapotranspiration estimates from remote sensing for irrigation water management. In: *Satellite-based Applications on Climate Change*. Springer, Dordrecht, pp. 195–216. https://doi.org/10.1007/978-94-007-5872-8_13.
- McCabe, M.F., Wood, E.F., 2006. Scale influences on the remote estimation of evapotranspiration using multiple satellite sensors. *Remote Sens. Environ.* 105 (4), 271–285. <https://doi.org/10.1016/j.rse.2006.07.006>.
- McVicar, T.R., Van Niel, T.G., Li, L., Hutchinson, M.F., Mu, X., Liu, Z., 2007. Spatially distributing monthly reference evapotranspiration and pan evaporation considering topographic influences. *J. Hydrol.* 338 (3–4), 196–220. <https://doi.org/10.1016/j.jhydrol.2007.02.018>.
- MDA Federal, 2004. Landsat GeoCover ETM+ 2000 Edition Mosaics Tile N-03-05.ETM-EarthSat-MrSID, 1.0. USGS, Sioux Falls, South Dakota, pp. 2000. ftp://ftp.glcf.umd.edu/glcf/Mosaic_Landsat/.
- Monteith, J.L., 1973. *Principles of Environmental Physics*. Elsevier, New York, pp. 241.
- Mu, Q., Zhao, M., Running, S.W., 2011. Improvements to a MODIS global terrestrial evapotranspiration algorithm. *Remote Sens. Environ.* 115 (8), 1781–1800. <https://doi.org/10.1016/j.rse.2011.02.019>.
- Pan, X.D., Li, X., 2013. The Atmospheric Forcing Data From 2000 to 2015 in the Heihe River Basin. Heihe Plan Science Data Center <https://doi.org/10.3972/heihe.019.2013.db>. <http://westdc.westgis.ac.cn/data/4022c086-8c3f-4f05-89eb-991468910f79> (The data set is provided by Cold and Arid Regions Sciences Data Center at Lanzhou (<http://westdc.westgis.ac.cn>)).
- Pan, X.D., Li, X., Shi, X.K., Han, X.J., Luo, L.H., Wang, L.X., 2012. Dynamic downscaling of near-surface air temperature at the basin scale using WRF-a case study in the Heihe River Basin, China. *Front. Earth Sci. China* 6 (3), 314–323. <https://doi.org/10.1007/s11707-012-0306-2>.
- Peng, Q., Xin, X., Jiao, J., Zhou, T., Liu, Q., 2016. Remote sensing algorithm for surface evapotranspiration considering landscape and statistical effects on mixed pixels. *Hydrol. Earth Syst. Sci.* 20 (11), 4409–4438. <https://doi.org/10.5194/hess-20-4409-2016>.
- Quan, J., Zhan, W., Ma, T., Du, Y., Guo, Z., Qin, B., 2018. An integrated model for generating hourly landsat-like land surface temperatures over heterogeneous landscapes. *Remote Sens. Environ.* 206, 403–423. <https://doi.org/10.1016/j.rse.2017.12.003>.
- Redelsperger, J.L., Thorncroft, C.D., Diedhiou, A., Lebel, T., Parker, D.J., Polcher, J., 2006. African monsoon multidisciplinary analysis: an international research project and field campaign. *Bull. Am. Meteorol. Soc.* 87 (12), 1739–1746. <https://doi.org/10.1175/BAMS-87-12-1739>.
- Ryu, Y., Baldocchi, D.D., Black, T.A., Dettò, M., Law, B.E., Leuning, R., et al., 2012. On the temporal upscaling of evapotranspiration from instantaneous remote sensing measurements to 8-day mean daily-sums. *Agric. For. Meteorol.* 152 (1), 212–222. <https://doi.org/10.1016/j.agrformet.2011.09.010>.
- Sandholt, I., Rasmussen, K., Andersen, J., 2002. A simple interpretation of the surface temperature/vegetation index space for assessment of surface moisture status. *Remote Sens. Environ.* 79 (2–3), 213–224. [https://doi.org/10.1016/S0034-4257\(01\)00274-7](https://doi.org/10.1016/S0034-4257(01)00274-7).
- Semmens, K.A., Anderson, M.C., Kustas, W.P., Gao, F., Alfieri, J.G., McKee, L., Prueger, J.H., Hain, C.R., Cammalleri, C., Yang, Y., Xia, T., Sanchez, L., Mar Alsina, M., Vélez,

- M., 2016. Monitoring daily evapotranspiration over two California vineyards using Landsat 8 in a multi-sensor data fusion approach. *Remote Sens. Environ.* 185, 155–170. <https://doi.org/10.1016/j.rse.2015.10.025>.
- Senay, G.B., Friedrichs, M.K., Singh, R.K., Velpuri, N.M., 2016. Evaluating Landsat 8 evapotranspiration for water use mapping in the Colorado River Basin. *Remote Sens. Environ.* 185, 171–185. <https://doi.org/10.1016/j.rse.2015.12.043>.
- Song, L., Liu, S., Kustas, W.P., Zhou, J., Xu, Z., Xia, T., Li, M., 2016. Application of remote sensing-based two-source energy balance model for mapping field surface fluxes with composite and component surface temperatures. *Agric. For. Meteorol.* 230–231, 8–19. <https://doi.org/10.1016/j.agrformet.2016.01.005>.
- Su, Z., 2002. The Surface Energy Balance System (SEBS) for estimation of turbulent heat fluxes. *Hydrol. Earth Syst. Sci.* 6 (1), 85–100. <https://doi.org/10.5194/hess-6-85-2002>.
- Su, Z., Schmugge, T., Kustas, W.P., Massman, W.J., 2001. An evaluation of two models for estimation of the roughness height for heat transfer between the land surface and the atmosphere. *J. Appl. Meteorol.* 40, 1933–1951. [https://doi.org/10.1175/1520-0450\(2001\)040%3C1933:AEOTMF%3E2.0.CO;2](https://doi.org/10.1175/1520-0450(2001)040%3C1933:AEOTMF%3E2.0.CO;2).
- Su, H., McCabe, M.F., Wood, E.F., Su, Z., Prueger, J.H., 2005. Modeling evapotranspiration during SMACEX: comparing two approaches for local-and regional-scale prediction. *J. Hydrometeorol.* 6 (6), 910–922. <https://doi.org/10.1175/JHM466.1>.
- Tang, R., Li, Z.L., Jia, Y., Li, C., Sun, X., Kustas, W.P., Anderson, M.C., 2011. An inter-comparison of three remote sensing-based energy balance models using Large Aperture Scintillometer measurements over a wheat–corn production region. *Remote Sens. Environ.* 115 (12), 3187–3202. <https://doi.org/10.1016/j.rse.2011.07.004>.
- Tang, R., Li, Z.L., Chen, K.S., Jia, Y., Li, C., Sun, X., 2013. Spatial-scale effect on the SEBAL model for evapotranspiration estimation using remote sensing data. *Agric. For. Meteorol.* 174–175, 28–42. <https://doi.org/10.1016/j.agrformet.2013.01.008>.
- Tanguy, M., Baillé, A., González-Real, M.M., Lloyd, C., Cappaëre, B., Kergoat, L., Cohard, J.-M., 2012. A new parameterisation scheme of ground heat flux for land surface flux retrieval from remote sensing information. *J. Hydrol.* 454–455, 113–122. <https://doi.org/10.1016/j.jhydrol.2012.06.002>.
- Timmermans, J., Su, Z., van der Tol, C., Verhoeven, A., Verhoef, W., 2013. Quantifying the uncertainty in estimates of surface–atmosphere fluxes through joint evaluation of the SEBS and SCOPE models. *Hydrol. Earth Syst. Sci.* 17 (4), 1561–1573. <https://doi.org/10.5194/hess-17-1561-2013>.
- Twine, T.E., Kustas, W.P., Norman, J.M., Cook, D.R., Houser, P., Meyers, T.P., Prueger, J.H., Starks, P.J., Wesely, M.L., 2000. Correcting eddy-covariance flux under-estimates over a grassland. *Agric. For. Meteorol.* 103 (3), 279–300. [https://doi.org/10.1016/S0168-1923\(00\)00123-4](https://doi.org/10.1016/S0168-1923(00)00123-4).
- van den Hurk, B.J.J.M., Holtslag, A.A.M., 1997. On the bulk parameterization of surface fluxes for various conditions and parameter ranges. *Bound.-Layer Meteorol.* 82 (1), 119–133. <https://doi.org/10.1023/A:100245600901>.
- van der Kwast, J., Timmermans, W., Gieske, A., Su, Z., Olioso, A., Jia, L., Elbers, J., Karssenberg, D., de Jong, S., 2009. Evaluation of the Surface Energy Balance System (SEBS) applied to ASTER imagery with flux-measurements at the SPARC 2004 site (Barax, Spain). *Hydrol. Earth Syst. Sci.* 13, 1337–1347. <https://doi.org/10.5194/hess-13-1337-2009>.
- van Halsema, G.E., Vincent, L., 2012. Efficiency and productivity terms for water management: a matter of contextual relativism versus general absolutism. *Agric. Water Manag.* 108, 9–15. <https://doi.org/10.1016/j.agwat.2011.05.016>.
- Van Niel, T.G., McVicar, T.R., Roderick, M.L., van Dijk, A.I.J.M., Renzullo, L.J., van Gorsel, E., 2011. Correcting for systematic error in satellite-derived latent heat flux due to assumptions in temporal scaling: assessment from flux tower observations. *J. Hydrol.* 409 (1–2), 140–148. <https://doi.org/10.1016/j.jhydrol.2011.08.011>.
- Van Niel, T.G., McVicar, T.R., Roderick, M.L., van Dijk, A.I.J.M., Beringer, J., Hutley, L.B., van Gorsel, E., 2012. Upscaling latent heat flux for thermal remote sensing studies: comparison of alternative approaches and correction of bias. *J. Hydrol.* 468–469, 35–46. <https://doi.org/10.1016/j.jhydrol.2012.08.005>.
- Wang, J., Zhuang, J., Wang, W., Liu, S., Xu, Z., 2015. Assessment of uncertainties in eddy covariance flux measurement based on intensive flux matrix of HiWATER-MUSOEXE. *IEEE Geosci. Remote Sens. Lett.* 12 (2), 259–263. <https://doi.org/10.1109/LGRS.2014.2334703>.
- Wang, W., Li, J., Yu, Z., Ding, Y., Xing, W., Lu, W., 2018. Satellite retrieval of actual evapotranspiration in the Tibetan Plateau: components partitioning, multidecadal trends and dominated factors identifying. *J. Hydrol.* 559, 471–485. <https://doi.org/10.1016/j.jhydrol.2018.02.065>.
- Wen, X., Yang, B., Sun, X., Lee, X., 2016. Evapotranspiration partitioning through in-situ oxygen isotope measurements in an oasis cropland. *Agric. For. Meteorol.* 230–231, 89–96. <https://doi.org/10.1016/j.agrformet.2015.12.003>.
- Weng, Q., Fu, P., Gao, F., 2014. Generating daily land surface temperature at Landsat resolution by fusing Landsat and MODIS data. *Remote Sens. Environ.* 145, 55–67. <https://doi.org/10.1016/j.rse.2014.02.003>.
- Wu, B., Yan, N., Xiong, J., Bastiaanssen, W.G.M., Zhu, W., Stein, A., 2012. Validation of ETWatch using field measurements at diverse landscapes: a case study in Hai Basin of China. *J. Hydrol.* 436–437, 67–80. <https://doi.org/10.1016/j.jhydrol.2012.02.043>.
- Wu, X., Zhou, J., Wang, H., Li, Y., Zhong, B., 2015. Evaluation of irrigation water use efficiency using remote sensing in the middle reach of the Heihe river, in the semi-arid Northwestern China. *Hydrol. Process.* 29 (9), 2243–2257. <https://doi.org/10.1002/hyp.10365>.
- WWAP (United Nations World Water Assessment Programme), 2016. The United Nations World Water Development Report 2016: Water and Jobs. UNESCO, Paris. <http://unesdoc.unesco.org/images/0024/002439/243938e.pdf>.
- Xiao, Q., Wen, J., 2013. HiWATER: Airborne LiDAR-DSM Data Production in the Middle Reaches of the Heihe River Basin. Cold and Arid Regions Science Data Center at Lanzhou <https://doi.org/10.3972/hiwater.149.2013.db>. <http://westdc.westgis.ac.cn/cn/hiwater/view/uid/b8e0b8f8-84d3-4735-b569-17b65b64cd8>.
- Xu, Z., Liu, S., Li, X., Shi, S., Wang, J., Zhu, Z., Xu, T., Wang, W., Ma, M., 2013. Intercomparison of surface energy flux measurement systems used during the HiWATER-MUSOEXE. *J. Geophys. Res. Atmos.* 118 (23), 13,140–13,157. <https://doi.org/10.1002/2013JD020260>.
- Xu, T., Liu, S., Xu, L., Chen, Y., Jia, Z., Xu, Z., Nielson, J., 2015. Temporal upscaling and reconstruction of thermal remotely sensed instantaneous evapotranspiration. *Remote Sens.* 7 (3), 3400–3425. <https://doi.org/10.3390/rs70303400>.
- Xu, Z., Ma, Y., Liu, S., Shi, W., Wang, J., 2017. Assessment of the energy balance closure under advective conditions and its impact using remote sensing data. *J. Appl. Meteorol. Climatol.* 56 (1), 127–140. <https://doi.org/10.1175/JAMC-D-16-0096.1>.
- Yan, C., 2011. Landuse/Landcover Data of Zhangye City in 2005. Heihe Plan Science Data Center <https://doi.org/10.3972/heihe.011.2013.db>. <http://westdc.westgis.ac.cn/data/9883313c-a69c-439a-92a1-8bd72ed92596>(The data set is provided by Cold and Arid Regions Sciences Data Center at Lanzhou (<http://westdc.westgis.ac.cn>)).
- Yang, K., Koike, T., Fujii, H., Tamagawa, K., Hirose, N., 2002. Improvement of surface flux parameterizations with a turbulence-related length. *Q. J. R. Meteorol. Soc.* 128 (584), 2073–2087. <https://doi.org/10.1256/003590002320603548>.
- Yang, K., Koike, T., Ishikawa, H., Kim, J., Li, X., Liu, H., Liu, S., Ma, Y., Wang, J., 2008. Turbulent flux transfer over bare-soil surfaces: characteristics and parameterization. *J. Appl. Meteorol. Climatol.* 47 (1), 276–290. <https://doi.org/10.1175/2007JAMC1547.1>.
- Yang, Y., Shang, S., Jiang, L., 2012. Remote sensing temporal and spatial patterns of evapotranspiration and the responses to water management in a large irrigation district of North China. *Agric. For. Meteorol.* 164, 112–122. <https://doi.org/10.1016/j.agrformet.2012.05.011>.
- Yang, G., Weng, Q., Pu, R., Gao, F., Sun, C., Li, H., Zhao, C., 2016. Evaluation of ASTER-like daily land surface temperature by fusing ASTER and MODIS data during the HiWATER-MUSOEXE. *Remote Sens.* 8, 75. <https://doi.org/10.3390/rs8010075>.
- Yu, X., Guo, X., Wu, Z., 2014. Land surface temperature retrieval from Landsat 8 TIRS—comparison between radiative transfer equation-based method, split window algorithm and single channel method. *Remote Sens.* 6 (10), 9829–9852. <https://doi.org/10.3390/rs6109829>.
- Zayed, I.S.A., Elagib, N.A., Ribbe, L., Heinrich, J., 2016. Satellite-based evapotranspiration over Gezira Irrigation Scheme, Sudan: a comparative study. *Agric. Water Manag.* 177, 66–76. <https://doi.org/10.1016/j.agwat.2016.06.027>.
- Zhang, R., Wang, J., Zhu, C., Sun, X., Zhu, Z., 2004. The retrieval of two-dimensional distribution of the earth's surface aerodynamic roughness using SAR image and TM thermal infrared image. *Sci. China Ser. D Earth Sci.* 47 (12), 1134–1146. <https://link.springer.com/article/10.1360/03yd0064> or <http://ir.igsnrr.ac.cn/handle/311030/3565>.
- Zhao, L.W., Ji, X.B., 2010. Quantification of transpiration and evaporation over agricultural field using the FAO-56 dual crop coefficient approach—a case study of the maize field in an oasis in the middle stream of the Heihe River Basin in Northwest China. *Sci. Agric. Sin.* 43 (19), 4016–4026. <http://www.chinaagrisci.com/CN/10.3864/j.issn.0578-1752.2010.19.014> or <http://www.chinaagrisci.com/CN/Y2010/V43/I19/4016>.
- Zhou, J., Chen, Y., Zhang, X., Zhan, W., 2013. Modelling the diurnal variations of urban heat islands with multi-source satellite data. *Int. J. Remote Sens.* 34 (21), 7568–7588. <https://doi.org/10.1080/01431161.2013.821576>.
- Zhou, Y.Z., Zhou, J., Li, Y., Wang, X.F., 2014. Simulating the evapotranspiration with SEBAL and Modified SEBAL(M-SEBAL) models over the desert and oasis of the middle reaches of the Heihe River. *J. Glaciol. Geocryol.* 36 (6), 1526–1537. <http://bcdt.westgis.ac.cn/EN/10.7522/j.issn.1000-0240.2014.0183> or <http://bcdt.westgis.ac.cn/EN/Y2014/V36/I16/1526>.
- Zhou, J., Dai, F., Zhang, X., Zhao, S., Li, M., 2015. Developing a temporally land cover-based look-up table (TL-LUT) method for estimating land surface temperature based on AMSR-E data over the Chinese landmass. *Int. J. Appl. Earth Obs. Geoinf.* 34, 35–50. <https://doi.org/10.1016/j.jag.2014.07.001>.
- Zhu, X., Chen, J., Gao, F., Chen, X., Masek, J.G., 2010. An enhanced spatial and temporal adaptive reflectance fusion model for complex heterogeneous regions. *Remote Sens. Environ.* 114 (11), 2610–2623. <https://doi.org/10.1016/j.rse.2010.05.032>.
- Zhu, X., Liu, D., Chen, J., 2012. A new geostatistical approach for filling gaps in Landsat ETM + SLC-off images. *Remote Sens. Environ.* 124, 49–60. <https://doi.org/10.1016/j.rse.2012.04.019>.
- Ziehn, T., Tomlin, A.S., 2009. GUI-HDMR – a software tool for global sensitivity analysis of complex models. *Environ. Model. Softw.* 24 (7), 775–785. <https://doi.org/10.1016/j.envsoft.2008.12.002>.